



CHORUS

This is the accepted manuscript made available via CHORUS. The article has been published as:

Coupling 2D atomistic information to 3D kink-pair enthalpy models of screw dislocations in bcc metals

Sicong He, Emma Overly, Vasily Bulatov, Jaime Marian, and David Cereceda

Phys. Rev. Materials **3**, 103603 — Published 15 October 2019

DOI: [10.1103/PhysRevMaterials.3.103603](https://doi.org/10.1103/PhysRevMaterials.3.103603)

Coupling 2D atomistic information to 3D kink-pair enthalpy models of screw dislocations in bcc metals

Sicong He,¹ Emma Overly,¹ Vasily Bulatov,² Jaime Marian,^{1,3,*} and David Cereceda⁴

¹*Department of Materials Science and Engineering,
University of California Los Angeles, Los Angeles, CA, USA*

²*Physical and Life Sciences Directorate, Lawrence Livermore National Laboratory, Livermore, CA, USA*

³*Department of Mechanical and Aerospace Engineering,
University of California Los Angeles, Los Angeles, CA, USA*

⁴*Department of Mechanical Engineering, Villanova University, Villanova, PA, USA*

(Dated: September 23, 2019)

The kink-pair activation enthalpy is a fundamental parameter in the theory of plasticity of body-centered cubic (bcc) metals. It controls the thermally activated motion of screw dislocation at low and intermediate temperatures. While direct atomistic calculations of kink-pairs on screw dislocations have reached a high degree of accuracy, they can only be practically performed using semiempirical interatomic force fields, as electronic structure methods have not yet reached the level of efficiency needed to capture the system sizes required to model kink-pair structures. In this context, an alternative approach based on standard three-dimensional elastic models, which are efficient but lack atomic-level information, coupled to a substrate potential that represents the underlying lattice, has been widely applied over the past few years. This class of methods, known as 'line-on-substrate' (LOS) models, uses the substrate potential to calculate the lattice contribution to the kink-pair energies. In this work, we introduce the stress-dependence of the substrate potential into LOS models to evaluate its impact on kink-pair energies. In addition, we present a new piece of dislocation physics in bcc metals, i.e. the observation of asymmetric dislocation core energies in the dislocation character space. This asymmetry is also elevated to the continuum level by adding core energies to the general LOS formulation, and used to explain potential energy differences known to exist between left and right kinks in bcc metals. More importantly, by matching the total LOS energies to previously calculated atomistic energies of kink-pair configurations, we issue a rule to establish the value of the so-called *core width* in non-singular elasticity theories, and reduce its arbitrariness as a mathematical construct.

* jmarian@ucla.edu

I. INTRODUCTION

30

31 In the field of dislocation physics, body-centered cubic (bcc) metals are peculiar due to the
 32 existence of non-planar dislocations with screw character and thermally-activated mobility that
 33 control plastic flow at low-to-intermediate temperatures. These dislocations have a Burgers vector
 34 \mathbf{b} equal to $\frac{1}{2}\langle 111 \rangle$ and move on close-packed planes (primarily $\{110\}$ and $\{112\}$) [1–5]. Generally,
 35 this motion is understood to occur over a periodic energy landscape known as the *Peierls* potential
 36 via the thermally activated nucleation of steps on the dislocation line, known as *kink pairs*, and
 37 their subsequent sideward relaxation [6–12]. Screw dislocations in bcc materials often behave in
 38 non-crystallographic ways, giving rise to phenomena such as pencil glide, asymmetry of the critical
 39 stress in the twinning and anti-twinning glide directions, asymmetry of the critical stress under
 40 tension/compression loading, or anomalous slip [13–23]. Most of these peculiarities are typically
 41 attributed to the highly compact (non-planar) structure of the $\frac{1}{2}\langle 111 \rangle$ screw dislocation core,
 42 which has naturally attracted much attention over the last several decades mostly in the form of
 43 atomistic models [24–26]. Based on recent work using electronic structure calculations, a picture
 44 has emerged whereby the preferred dislocation core structure in bcc crystals has been established
 45 to be a compact, non-dissociated core resting on an underlying sinusoidal Peierls potential, U_P
 46 [27–31].

47 The strong temperature dependence of the yield and flow stresses displayed by most bcc metals
 48 is generally rationalized in terms of the thermally-activated nature of kink-pair nucleation. As
 49 such, a principal objective of the materials community in bcc alloys has been to develop models to
 50 characterize the activation energy of kink pairs. These are typically based on energy minimization
 51 of curved string configurations lying on a static energy substrate in either one [32, 33] or two
 52 dimensions [34]. The energy of the string is obtained by solving an integro-differential equation
 53 in a two-dimensional space defined by the glide x and screw z directions that accounts for the
 54 elastic energy of the line, its position on the substrate potential, and the mechanical work done by
 55 the stress τ [35, 36]. These so-called *line-on-substrate* (LOS) approaches have been traditionally
 56 approximated by models that reduce the double line integral (along x and z) to discrete sums along
 57 one or both integration dimensions. In the so-called line-tension (LT) model the integral along the
 58 screw direction is replaced by a dislocation self-energy which depends on the curvature of the line.
 59 The other integral is solved along the glide coordinate, yielding the equilibrium shape of the kink-
 60 pair configuration on the substrate potential. These activated configurations are usually referred to
 61 as ‘bulge’ structures as they resemble a protuberance on the dislocation line projected along the glide
 62 direction. The LT approach works well when this protuberance is small, i.e. at high and intermediate
 63 stresses¹, but not at low stresses when the equilibrium position of the line is near the minimum of
 64 potential energy U_P [32, 33]. For low values of τ , the elastic interaction (EI) between kinks governs
 65 the line energy, in which case one can approximate the bulge configuration by a polygon (typically
 66 a trapezoid) with mutually-interacting elastic segments, reducing the double integral to a set of
 67 discrete convergent sums [37, 38]. While this is a general consideration, irrespective of the material
 68 and the dislocation type, the case of screw dislocations in tungsten does not really follow this idea.
 69 This is because non-screw segment of the trapezoid are highly tilted towards the screw character
 70 (which is a consequence of the core energy values and not uncommon in bcc metals).

71 While insights gained from these models have improved our understanding of the activated states
 72 of kink-pair configurations, knowledge obtained from a decade or so of atomistic calculations sup-

¹ While the terms ‘low’ and ‘high’ stress used throughout this paper is somewhat arbitrary, here, for reference, we have decided to assign a value of $0.25\sigma_P$ as the high limit of the low stress region, and $0.75\sigma_P$ as the low limit of the high stress region.

ports the need to augment LOS models with inelastic contributions brought about by non-linear effects of atomistic nature. The most important of these are (i) the alteration of the Peierls potential energy function in the presence of resolved shear stress, and (ii) the consideration of core energies into the energy description of kink-pair configurations. At low stresses, one can safely assume that U_P remains unchanged and the effect of stress on the dislocation can be linearly decoupled from the underlying substrate in the form of a mechanical work. However, at stresses approaching the critical stress, referred to as the *Peierls* stress τ_P at 0 K, it is insufficient to consider only the zero stress internal energy to represent the Peierls trajectory. This trajectory is defined as the rectilinear path, denoted by the reaction coordinate x , between two equivalent equilibrium states (known as ‘easy core’) on the Peierls potential, which has periodicity $h_0 = a_0 \frac{\sqrt{6}}{3}$, where a_0 is the lattice constant. As recent calculations have shown, U_P can couple to the applied stress in non-negligible ways [39]. For its part, the inelastic contribution to the total dislocation energy, referred to as the *core* energy, is known to be potentially an important driving force in the minimization of dislocation line configurations (e.g. the so-called *self-force* in dislocation dynamics models). In particular, as will be shown below, in bcc metals the dependence of the core energy with dislocation character is periodic in the entire $[-\frac{\pi}{2}, \frac{\pi}{2}]$ angular range of θ (taken to be equal to zero for the screw orientation), contrary to other crystal structures, which display a $[0, \frac{\pi}{2}]$ periodicity. While this is a consequence of a well-known asymmetry of the bcc crystal lattice [4, 15, 16], it has not been included into continuum models of kink-pair configurations to date.

In this work, we explore the effect of these features on numerical LT and EI models of kink-pair configurations modified to account for variations in $U_P(x)$ brought about by the applied stress and character-dependent dislocation core energies. Ultimately, we are **testing the notion of whether** atomistic information based on (quasi) 2D simulations can be effectively integrated into dislocation energy models of 3D line configurations is correct to interpret bcc plastic behavior. As well, we check whether fine details obtained in atomistic models, such as, e.g., the energy asymmetry between left and right-handed kinks that has been observed in several bcc metals [40–42], can be accurately captured by this coupled approach. Our paper is organized as follows. First we introduce the unprocessed physical inputs as obtained from atomistic simulations. Next, we review the theoretical formulation of the EI and LT models employed here. This is followed by details about the coupling between atomistic information and the discretized continuum models. We then show results for two different atomistic force fields for tungsten. We conclude the paper with a discussion of the results and some general conclusions.

II. RAW ATOMISTIC INPUTS

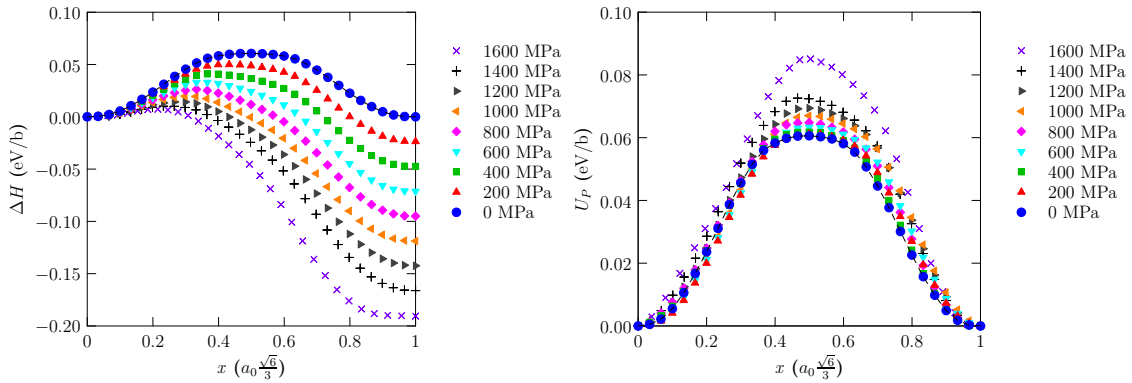
Based on a prior analysis of several W interatomic potentials for screw dislocation property calculations [43], we have selected an embedded-atom method (EAM) [44] and a *modified*-EAM (MEAM) potential [45] as the most suitable in terms of physical accuracy and computational efficiency. Using these two potentials, we have studied the dependence of $U_P(x)$ on the resolved shear stress, and of the dislocation core energies on dislocation character. This furnishes what we refer to as ‘raw’ atomistic inputs, i.e. before they are processed to be in usable form for the LOS models.

113

1. Peierls potential

114 The Peierls potential $U_P(x)$ is obtained as the minimum energy path along the reaction co-
 115 ordinate x joining two adjacent equilibrium dislocation core configurations (known as *easy* core
 116 configurations). This is done using the *nudged elastic band* (NEB) method [46] in small atomistic
 117 supercells reflecting the structure of balanced dipole configurations oriented along the $[111]$, $[\bar{1}2\bar{1}]$
 118 and $[\bar{1}01]$ directions, **corresponding, respectively, to the x , y and z directions**. These configurations
 119 permit the use of periodic boundary conditions along all three supercell directions. The dimensions
 120 of the simulation cell along the three coordinate axes were $L_x = 13.6 \text{ \AA}$ ($5b$), $L_y = 108 \text{ \AA}$, and $L_z =$
 121 107 \AA , containing a total of $N = 10000$ atoms. The NEB trajectory is partitioned into 30 images
 122 constrained to relax in configurational hyperplanes defined by the normal axis along x ($3N - 1$
 123 degrees of freedom).

124 Prior to the NEB calculations, unconstrained energy minimizations using LAMMPS [47] were carried
 125 out for the initial and final configurations. NEB trajectories are generated as a function of stress
 126 τ (resolved shear stress on the glide plane) and the results are shown in Fig. 1. The paths shown



127 FIG. 1. Variation of (a) **the enthalpy** and (b) the Peierls potential with stress for the EAM potential.
 128 Graphs (a) and (b) are connected by the term $-\tau b$, which is subtracted to the enthalpy to obtain U_P .

129 in the figure are generated by subtracting from the resulting NEB trajectory the mechanical work,
 130 $-\tau b x$, for each image and matching the equilibrium position, $x_0(\tau)$, and the associated energy in
 131 each case to the origin of each curve.

132

2. Dislocation core energies

133 The dislocation core energy is a mathematical construct designed to remove the singularity in
 134 the stress and strain fields of elasticity theory. As such, the core region is eminently *inelastic* in
 135 nature and can arbitrarily be defined by a parameter a referred to as the *core width*. This effectively
 136 partitions the total energy of a dislocation dipole into elastic and inelastic parts, with the latter
 137 confined to the core region within a [48–50] (cf. Section III A 2). This partition results in the
 138 following definition of the core energy:

$$139 \quad e_c(\theta, a) = \frac{e_{\text{atm}}(\theta) - e_{\text{el}}(\theta, a)}{2} \quad (1)$$

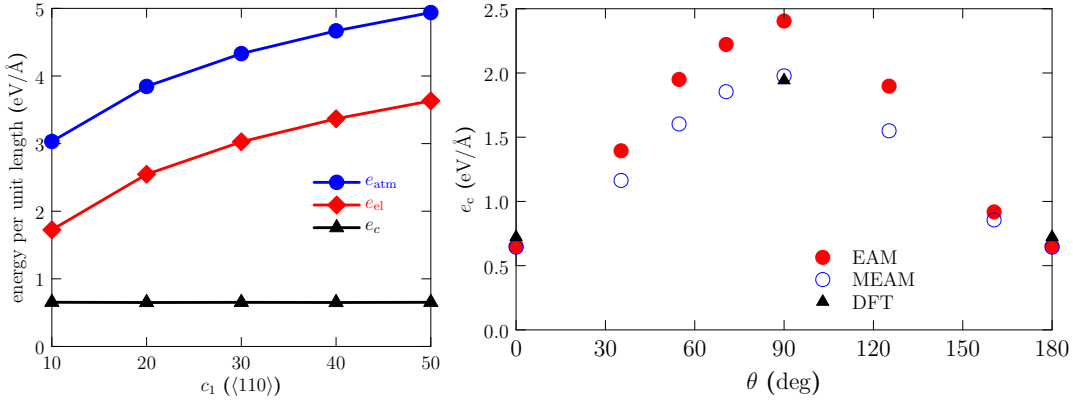


FIG. 2. Core energies obtained from atomistic simulations. (Left) Total atomistic energy (per unit length) for a computational cell containing a screw dislocation segment modeled with the EAM potential. The total energy is partitioned between an elastic energy and a core energy assuming a value of $a = 2b$. c_1 represents the size of the box along a $\langle 110 \rangle$ crystallographic direction (separation of the dislocation dipole). (Right) Dislocation core energies as a function of the character angle θ all for $a = 2b$. Results for both interatomic potentials, as well as DFT data, are shown.

140 where the angle $\theta = \cos^{-1}(\frac{\mathbf{b} \cdot \mathbf{t}}{b})$ formed by the Burgers vector \mathbf{b} and the line direction \mathbf{t} defines the
 141 dislocation character, while the $1/2$ factor reflects the existence of a dislocation dipole.

142 The total energy e_{atm} is obtained from conjugate gradient minimizations of periodic atomistic
 143 supercells containing a dislocation dipole much in the manner described in the above section. The
 144 only difference resides in the orientation of the supercell, whose axes z , y and x are now oriented
 145 along the \mathbf{n} , \mathbf{t} and $(\mathbf{n} \times \mathbf{t})$ directions, respectively. For its part, the elastic energy e_{el} is calculated by
 146 subtracting the interaction energy due to the periodic dipole network (appearing by virtue of using
 147 periodic boundary conditions) from the elastic energy of a dislocation dipole. An example of the
 148 partition of energy described by eq. (1) is shown in Figure 2. The core energies assuming a value of
 149 $a = 2b$ for the EAM and MEAM potentials, as well as for DFT calculations of pure screw (0°) and
 150 edge (90°) configurations [51] are also given in Figure 2. As the graph shows, the angular periodicity
 151 of the core energy function is $(0, \pi)$, as there is an asymmetry in the energies about the pure edge
 152 orientation. This is not surprising, given the natural crystallographic asymmetry of the bcc lattice,
 153 which is most notoriously manifested in the existence of the so-called M111 dislocation orientation
 154 [52]. As will be discussed later, this asymmetry in the core energies leads to different energies for
 155 ‘left’ and ‘right’-handed kinks, a phenomenon commonly observed in atomistic calculations using
 156 a number of interatomic potentials [40–42]. Further details about this geometric particularity are
 157 provided in Appendix B.

158 III. GENERAL THEORY OF THE LINE-ON-SUBSTRATE MODEL

159 Line-on-substrate model regards the dislocation as a line resting on a periodic energy landscape
 160 (substrate) that reflects the coupling between the dislocation line and the crystal lattice. As men-
 161 tioned in Sec. I, the two most widely used versions of the LOS model are the elastic interaction
 162 (EI) model and the line tension (LT) model. Here we provide a description of the theoretical

163 formulations employed here for each of the two cases.

164

A. Elastic interaction model

In the EI model, a kink-pair on a screw dislocation line can be approximated by an open trapezoid connected to two semi-infinite segments in the manner shown in Fig. 3: The segments LA and DR

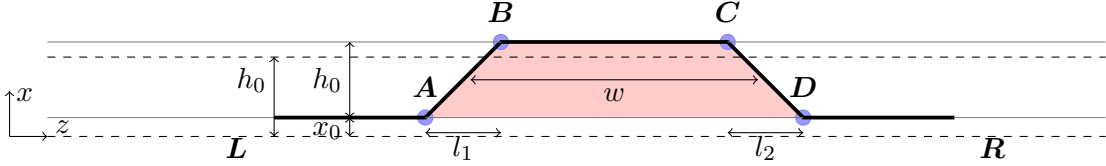


FIG. 3. Schematic representation of a kink-pair configuration on a straight screw dislocation. The points labeled L and R represent arbitrarily distant locations to the left and right of A and D , respectively. We use a cartesian coordinate system such that the x direction is along the glide direction, the y direction is normal to the glide plane, and z is oriented along the line. x_0 is the equilibrium position of a straight screw segment at a finite stress τ , defined in equation (12). h_0 is the periodicity of the Peierls potential, w is the distance between kinks, and l_1 and l_2 are the widths of the kinks (projections of the AB and CD segments on x). The shaded region corresponds to the slipped area defined in eq. (4).

are located on the first Peierls valley, the segment BC is on the second Peierls valley, and AB and CD are the kink segments that straddle both minima. w is the width of the trapezoid, which we take to be the distance between kinks, calculated as the distance between the two midpoints of segments AB and CD . l_1 and l_2 are the widths (along the z direction) of such two segments, calculated as the z -distance between the point at $x = 0.05h_0 + x_0$ and that at $x = 0.95h_0 + x_0$. One can use the structure shown in Fig. 3 to obtain stable configurations for the activated state by optimizing the activation enthalpy of the system for a given stress. The activated state can be characterized by the sum of self-energies ΔE_{self} and interaction energies ΔE_{int} for all segments shown in the figure. In addition, the contribution to the energy of the underlying substrate ΔU_{P} must be separately considered for the case of screw dislocations in bcc metals. The enthalpy is then obtained by subtracting the mechanical work W_m performed by the stress τ from the three contributions mentioned above:

$$\Delta H(\{\mathbf{r}_i\}, \tau) = \Delta E_{\text{self}}(\{\mathbf{r}_i\}, \theta_i) + \Delta E_{\text{int}}(\{\mathbf{r}_i\}) + \Delta U_{\text{P}}(\{\mathbf{r}_i\}) - W_m(\tau, \{\mathbf{r}_i\}) \quad (2)$$

165 The stable configurations for the kink-pair structure shown in the figure are obtained by opti-
 166 mizing the above expression with respect to the coordinates \mathbf{r}_A , \mathbf{r}_B , \mathbf{r}_C , \mathbf{r}_D . Note that, due to
 167 the asymmetry in the e_c function described in the previous Section, in Fig. 3 the kink widths l_1
 168 and l_2 do not necessarily have to be equal. This sets our work apart from other studies where it is
 169 commonly assumed that they are the same [30, 38]. The energies of the kink-pair configurations
 170 shown in the figure need to be computed piecewise, adding the contributions from all the dislocation
 171 segments. In the next sections we provide expressions for each of the energy terms introduced in
 172 eq. (2).

173 *1. The mechanical work*

174 The mechanical work W_m in eq. (2) is simply defined as:

$$175 \quad W_m(\tau, \{\mathbf{r}_i\}) = \tau b A \quad (3)$$

176 where τ , b , and A are, respectively, the resolved stress on the glide plane, the magnitude of the
177 Burgers vector, and the area swept by the kink pair. This area can be calculated as:

$$178 \quad A = \frac{1}{2} (|\mathbf{AB} \times \mathbf{AC}| + |\mathbf{DC} \times \mathbf{DA}|) \quad (4)$$

179 *2. Self-energies of dislocation segments*

In accordance with Hirth and Lothe [36] and Koizumi *et al.* [38], the total elastic self-energy of the configuration in Fig. 3 can be written as:

$$\Delta E_{\text{self}}^{\text{el}}(\{\mathbf{r}_i\}) = E_{\text{self}}^{\text{el}}(\mathbf{AB}) + E_{\text{self}}^{\text{el}}(\mathbf{BC}) + E_{\text{self}}^{\text{el}}(\mathbf{CD}) - E_{\text{self}}^{\text{el}}(\mathbf{AD}) \quad (5)$$

180 Here we use the non-singular expressions for the self-energy of a straight dislocation segment \mathbf{m}
181 defined by endpoints \mathbf{r}_1 and \mathbf{r}_2 , and Burgers vector \mathbf{b} provided by Cai *et al.* [53], which give these
182 energies as a function of θ and a . In this work, we add the core energy contribution to the above
183 elastic energies as:

$$184 \quad E_{\text{self}}(\mathbf{m}) = E_{\text{self}}^{\text{el}}(\mathbf{m}) + e_c(\theta, a) \|\mathbf{m}\| \quad (6)$$

185 *3. Interaction energies*

For the interaction energies, Hirth and Lothe [36] give the following expression for a symmetric kink-pair.

$$\begin{aligned} \Delta E_{\text{int}}(\{\mathbf{r}_i\}) = & \\ & 2 [E_{\text{int}}(\mathbf{LA}/\mathbf{AB}) + E_{\text{int}}(\mathbf{LA}/\mathbf{BC}) + E_{\text{int}}(\mathbf{LA}/\mathbf{CD}) + E_{\text{int}}(\mathbf{AB}/\mathbf{BC}) - E_{\text{int}}(\mathbf{LA}/\mathbf{AD})] + \\ & + E_{\text{int}}(\mathbf{AB}/\mathbf{CD}) \end{aligned} \quad (7)$$

where, by symmetry, the following equivalences can be established:

$$E_{\text{int}}(\mathbf{LA}/\mathbf{AB}) \equiv E_{\text{int}}(\mathbf{DR}/\mathbf{CD})$$

$$E_{\text{int}}(\mathbf{LA}/\mathbf{BC}) \equiv E_{\text{int}}(\mathbf{DR}/\mathbf{BC})$$

$$E_{\text{int}}(\mathbf{LA}/\mathbf{CD}) \equiv E_{\text{int}}(\mathbf{DR}/\mathbf{AB})$$

$$E_{\text{int}}(\mathbf{AB}/\mathbf{BC}) \equiv E_{\text{int}}(\mathbf{CD}/\mathbf{BC})$$

$$E_{\text{int}}(\mathbf{LA}/\mathbf{AD}) \equiv E_{\text{int}}(\mathbf{DR}/\mathbf{AD})$$

However, for an asymmetric configuration, only the last one is true and, thus, the sum of interaction energies reads:

$$\begin{aligned} \Delta E_{\text{int}}(\{\mathbf{r}_i\}) &= E_{\text{int}}(\mathbf{LA}/\mathbf{AB}) + E_{\text{int}}(\mathbf{DR}/\mathbf{CD}) \\ &+ E_{\text{int}}(\mathbf{LA}/\mathbf{BC}) + E_{\text{int}}(\mathbf{DR}/\mathbf{BC}) + E_{\text{int}}(\mathbf{LA}/\mathbf{CD}) + \\ &+ E_{\text{int}}(\mathbf{DR}/\mathbf{AB}) + E_{\text{int}}(\mathbf{AB}/\mathbf{BC}) + E_{\text{int}}(\mathbf{CD}/\mathbf{BC}) \\ &- 2E_{\text{int}}(\mathbf{LA}/\mathbf{AD}) + E_{\text{int}}(\mathbf{AB}/\mathbf{CD}) \end{aligned} \quad (8)$$

The general expression within non-singular isotropic elasticity theory for the interaction energy of two segments \mathbf{m} and \mathbf{n} with, respectively, endpoints \mathbf{r}_1 and \mathbf{r}_2 , and \mathbf{r}_3 and \mathbf{r}_4 is:

$$E_{\text{int}}(\mathbf{m}, \mathbf{n}) = E^*(\mathbf{r}_4 - \mathbf{r}_2) + E^*(\mathbf{r}_3 - \mathbf{r}_1) - E^*(\mathbf{r}_4 - \mathbf{r}_1) - E^*(\mathbf{r}_3 - \mathbf{r}_2) \quad (9)$$

186 where the functional E^* takes different forms depending on the nature of the interaction. The
187 non-singular elastic expressions used here to obtain E^* are all given by Cai *et al.* [53], which we
188 include in Appendix C, in case they could be valuable for the reader.

189 4. The Peierls potential

190 The kink pair structure shown in Fig. 3 rests on a periodic energy landscape known as the Peierls
191 potential, U_{P} . Multiple atomistic studies using DFT and semi-empirical potentials [54–56] have
192 shown that U_{P} is well represented by a (co)sinusoidal function of the type:

$$193 \quad U_{\text{P}}(x) = \frac{U_0}{2(1-\alpha)} \left[1 - \cos \frac{2\pi x}{h_0} - \frac{\alpha}{2} \left(1 - \cos \frac{2\pi x}{h_0} \right)^2 \right] \quad (10)$$

194 where x represents the reaction coordinate (along the glide direction), U_0 is known as the Peierls
195 energy, and h_0 is the period of U_{P} ($h_0 = a_0\sqrt{6}/3$ in bcc lattices). α is a parameter that captures
196 the deviation of U_{P} from a pure cosine function. The contribution to the total energy of a kink
197 segment lying across two Peierls valleys is:

$$198 \quad \Delta U_{\text{P}}(\{\mathbf{r}_i\}) = \int_{\mathbf{LABCDR}} U_{\text{P}}(x) d\ell - \int_{\mathbf{LADR}} U_{\text{P}}(x) d\ell \quad (11)$$

199 Both of the above integrals are evaluated from an equilibrium position x_0 to $x_0 + h_0$. x_0 is obtained
200 from the following relation:

$$201 \quad \left. \frac{dU_{\text{P}}(x)}{dx} \right|_{x=x_0} = \tau b \quad (12)$$

The infinitesimal differential $d\ell$ follows along the kink segment and can be linearized as:

$$d\ell = \sqrt{dx^2 + dz^2}$$

202 We now make the approximation that the straight segments \mathbf{LA} , \mathbf{BC} , \mathbf{DR} cancel with their
203 respective counterparts in the \mathbf{LADR} configuration. Then the above integrals reduce to:

$$204 \quad \Delta U_{\text{P}}(\{\mathbf{r}_i\}) = \int_{x_0}^{x_0+h_0} U_{\text{P}}(x) (d\ell_1 + d\ell_2) - U_{\text{P}}(x_0) (l_1 + l_2) \quad (13)$$

205 To capture the effect of the resolved shear stress on the shape of $U_P(x)$ revealed in Sec. II 1, we
 206 consider a stress dependence of both $U_0(\tau)$ and $\alpha(\tau)$, as will be shown in Appendix A.

Equations (3), (5), (8), and (13) are combined to fully define the activation enthalpy in eq. (2), which is subsequently optimized for the set of parameters w , l_1 , and l_2 as a function of stress. Each saddle point corresponds to the activated state of the kink-pair at each stress, from which the dependence of $\Delta H(w, l_1, l_2)$ with τ can be calculated. The dimensions of the trapezoid corresponding to each optimized configuration are obtained as:

$$\begin{aligned}\mathbf{r}_A &\equiv (x_0, 0) \\ \mathbf{r}_B &\equiv (x_0 + h_0, l_1) \\ \mathbf{r}_C &\equiv (x_0 + h_0, l_1 + w) \\ \mathbf{r}_D &\equiv (x_0, l_1 + w + l_2)\end{aligned}$$

207

B. The line tension model as a simplified LOS approach

208 At low stresses the stability of the kink-pair configuration is controlled by the elastic interaction
 209 between the kink segments. However, as the stress increases and the shape of the line resembles
 210 more a ‘bulged’ structure with low curvature. In such cases, the elastic energy of the system is well
 211 approximated by a so-called *line tension* representation [57, 58], where the energy of the kink-pair
 212 structure is controlled by the curvature of non-straight segments. Within elasticity, the line tension
 213 is defined as:

$$214 \quad T(\theta, a) = \frac{\partial E_{\text{self}}(\theta, a)}{\partial \ell} \quad (14)$$

which is the dislocation energy per unit length, depending only on dislocation character θ and the core width a . For small dislocation segment lengths, ℓ , the above expression can be approximated by $T(\theta, a) \approx \frac{E_{\text{self}}(\theta, a)}{\ell}$. This form of $T(\theta, a)$ replaces the self and interaction elastic energies in the enthalpy expression for the kink-pair configuration. $\Delta H(\{\mathbf{r}_i\})$ now reads:

$$\Delta H(z, \tau) = \int dz [\Delta T(\theta(z), a) + \Delta e_c(\theta(z), a) + \Delta U_P(x(z), \tau) - W_m(\tau)] = \quad (15)$$

$$= \int dz [(T(\theta(z), a) - T(\theta = 0, a)) + (e_c(\theta(z), a) - e_c(\theta = 0, a)) + \Delta U_P(x(z), \tau) - W_m(\tau)] \quad (16)$$

215 where e_c , W_m and ΔU_P are defined as in Secs. II 2, III A 1 and III A 4. Eq. (15) can be represented
 216 as a piecewise sum along the z direction of the contributions of individual segments of length b [59]:

217

$$\Delta H(\{x_i\}, \tau) = b \sum_i \left[T(\theta_i, a) - T(\theta = 0, a) + (e_c(\theta_i, a) - e_c(\theta = 0, a)) + \Delta U_P(x_i, \tau) - \frac{\tau b}{2}(x_{i+1} + x_i - 2x_0) \right] \quad (17)$$

218

219 where $U_P(x, \tau)$ is given by equation (10), and $\theta_i = \tan^{-1} \left(\frac{x_{i+1} - x_i}{b} \right)$. The geometry of one dis-
 220 cretization segment is shown in Fig. 4 for the calculation of the mechanical work.

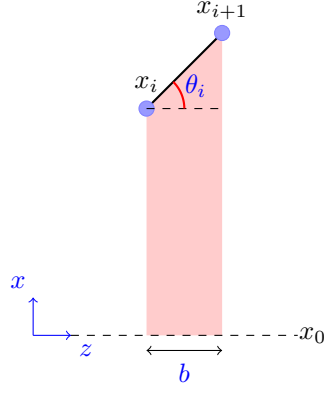


FIG. 4. Representation of a discrete segment used to calculate the enthalpy of the kink-pair configuration using the line tension LOS model. x_0 is calculated as in eq. (12).

The expression utilized in eq. (14) is derived from those provided by Cai *et al.* [53], which expressed in piecewise form for use in eq. (17) is:

$$T(\theta, a) = \frac{\mu b^2}{4\pi(1-\nu)} \left\{ (1 - \nu \cos^2 \theta) \ln \frac{b + \sqrt{b^2 + a^2}}{a} - \frac{3 - \nu}{2} \left(\frac{\sqrt{b^2 + a^2} - a}{b} \right) \cos^2 \theta \right\} \quad (18)$$

222 The equilibrium configurations are obtained by minimizing the value of ΔH in eq. (17) as a function
223 of the set of coordinates $\{x_i\}$ at each stress point τ .

224 IV. IMPLEMENTATION AND PARAMETERIZATION OF LOS MODELS

225 In this section we explain how to process the atomistic results described in Sec. II for use in the
226 EI and LT models just presented. First, we discuss the expressions for the stress-dependence of the
227 Peierls potential, followed by those pertaining to the core energies.

228 A. The Peierls potential

For the EI model, the integral in eq. (13) can be solved analytically and used directly in expression (2):

$$\begin{aligned} \Delta U_P(\{\mathbf{r}_i\}) &= \left(\sqrt{1 + \frac{l_1^2}{h_0^2}} + \sqrt{1 + \frac{l_2^2}{h_0^2}} \right) \int_{x_0}^{x_0+h_0} U_P(x) dx - U_P(x_0) (l_1 + l_2) = \\ &= \frac{U_0}{2(1-\alpha)} \left\{ \left(\sqrt{1 + \frac{l_1^2}{h_0^2}} + \sqrt{1 + \frac{l_2^2}{h_0^2}} \right) \left[h_0 \left(1 - \frac{3\alpha}{4} \right) + \right. \right. \\ &\quad \left. \left. - \frac{h_0(1-\alpha)}{2\pi} \left(\sin \frac{2\pi(x_0+h_0)}{h_0} - \sin \frac{2\pi x_0}{h_0} \right) - \frac{h_0\alpha}{16\pi} \left(\sin \frac{4\pi(x_0+h_0)}{h_0} - \sin \frac{4\pi x_0}{h_0} \right) \right] + \right. \\ &\quad \left. - (l_1 + l_2) \left[1 - \cos \frac{2\pi x}{h_0} - \frac{\alpha}{2} \left(1 - \cos \frac{2\pi x}{h_0} \right)^2 \right] \right\} \quad (19) \end{aligned}$$

229 where we have used $dz_\beta = \frac{l_\beta}{h_0} dx$, with $\beta = 1, 2$. The atomistic information provided in Sec. II 1
 230 has been introduced into this expression in the form of stress-dependent correlations for U_0 and α .
 231 We have seen that U_0 scales as τ^n whereas α is a linear function of τ . The specific expressions and
 232 the fitting procedure followed to obtain these correlations is described in Appendix A.

233 For the LT model, $U_P(x_i)$ is evaluated directly using (10) for each discretized segment x_i . Sum-
 234 mation over all segments then gives us the total potential energy of the line, in accordance with
 235 eq. (17). The expressions for $U_0(\tau)$ and $\alpha(\tau)$ are identical to those used in the EI model.

236 B. Core energies

237 The core energy results from atomistic calculations shown in Sec. II 2 are introduced in the same
 238 manner in the EI and LT models. In principle, the main features of e_c that a fitting procedure must
 239 capture are its dependence of both dislocation character (i.e. angle θ) and core width a . However,
 240 what is novel in this work is the slight asymmetry about the edge character orientation displayed
 241 in Fig. 2. For this, we additively separate the total core energy into an a -independent term, and
 242 an a -dependent one:

$$243 \quad e_c(\theta, a) = f(\theta) + g(\theta) \log\left(\frac{a}{b}\right) \quad (20)$$

244 where $f(\theta)$ and $g(\theta)$ are obtained by fitting the data in Fig. 2 to Fourier series expansions of the
 245 type:

$$246 \quad y(\theta) = c_0 + \sum_{k=1}^3 c_k \sin(2k\theta) + d_k \cos(2k\theta) \quad (21)$$

247 These functions can yield the asymmetry about $\theta = \pi/2$ and naturally satisfy the condition that
 248 their first derivative is equal to zero for $\theta = 0$ and $\theta = \pi$ (zero self-force for screw orientation).
 249 It is important to clarify that this partition of the core energy is mathematically arbitrary, and
 250 other works have opted for different approaches [60]. The dependence of the dislocation core energy
 251 with both the character angle and the core size is shown in Fig. 5. The details about the fitting
 252 procedure and the numerical values of the coefficients c_k and d_k are given in Appendix B.

254 C. Implementation details

255 1. Elastic interaction model

256 In the EI model, the kink-pair configuration itself represents the activated state between the two
 257 minima in the Peierls potential representing the initial and final screw dislocation configurations.
 258 As such, the enthalpy in eq. (2) must be maximized along the reaction path. This is done by
 259 obtaining the saddle point of the entire structure as a function of the position of points A , B ,
 260 C , and D in Fig. 3. However, standard (unconstrained) optimization algorithms are difficult to
 261 stabilize in an energy landscape that is only conditionally convergent [61]. The geometry of the
 262 configuration, however, can be used to identify conditions that favor convergence.

263 This can be done, for example, by noting that the trapezoid depicted in Fig. 3 represents a
 264 dislocation loop (with three ‘real’ segments and one ‘anti’ segment) whose elastic energy is known

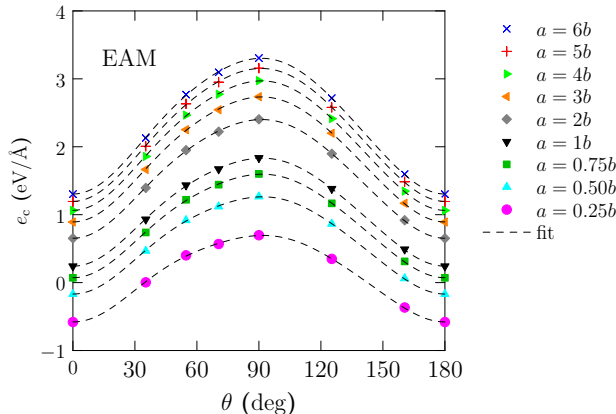


FIG. 5. Dislocation core energies for EAM interatomic potentials as a function of the dislocation character angle θ and the core size a . The curves generated using eq.(20) for nine different values of a are also plotted.

265 to be finite. This imposes limits on the minimum and maximum size of the trapezoidal structure
 266 that are discussed below.

267 (i) The condition of finite energy means that the total activation enthalpy in eq. (2) is independent
 268 of the size of segments LA and DR . Using isotropic singular linear elasticity, the terms
 269 depending on the lengths of these segments are seen to cancel in the analytical expressions for
 270 the total elastic energy of the trapezoidal configuration. With the non-singular theory, things
 271 are not quite as simple, as analytical expressions are not straightforward to obtain. However,
 272 the same premise must still hold. Here, we have performed a numerical study to confirm
 273 this, and have established the minimum length of segments LA and DR to have converged,
 274 length-independent energies. Figure 6 shows the combined value of $(\Delta E_{\text{int}} + \Delta E_{\text{self}})$ in eq. (2)
 275 as a function of the value of $\|LA\| \equiv \|RD\|$. Our results show that values of approximately
 276 $200b$ or larger must be used to achieve length independence. In most simulations, we have
 277 typically used a value of $1000b$.

279 (ii) At the same time, the separation of segments AB and CD (i.e. the value of w in Fig. 3)
 280 must be sufficiently small for the elastic interaction energy to be finite within the numerical
 281 tolerance of our minimization procedure. w changes with stress, but we have found that, as
 282 a rule of thumb, at zero stress, values of no less than $40b$ should be considered.

283 2. Line tension model

284 The case of the LT model differs from that of the EI model just explained. In this case, the saddle
 285 point configuration corresponds to a bulged structure that lies somewhere along the x coordinate.
 286 This configuration does not generally correspond to one where the line lies on either of the minima
 287 of U_P . Therefore, one must vary the size of the bulge, defined by a variable h along the x path
 288 between x_0 and h_0 until the system's enthalpy goes through a maximum. At each stress, this path
 289 is discretized and the saddle point structure found. This is expected to yield minimum energy paths
 290 that are substantially equivalent to dynamic trajectories [62]. To improve the rate of convergence,

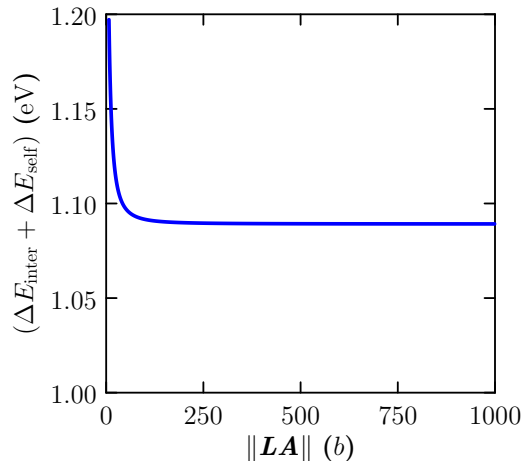


FIG. 6. Elastic interaction and self energies as a function of the length of LA and DR segments.

291 here we invert the potential energy landscape by altering the sign of the mechanical work along
 292 the path as to balance the rest of the terms in the enthalpy and have net zero effect on the total
 293 energy. This approach has proven robust for the calculations undertaken in this work.

294 Once the saddle-point configuration is found for each stress, we approximate the left and right
 295 sides of the bulged structure with an arc tangent function. All the corresponding outputs (i.e. w ,
 296 l_1 , l_2 , etc) are calculated upon mathematical analysis of the best approximants obtained for each
 297 case.

298 V. RESULTS

299 The first-principles method used here for parameterizing and benchmarking the LOS model
 300 calculations are atomistic calculation results using two different interatomic potentials, EAM and
 301 MEAM. All atomistic calculations were done using molecular statics at 0 K. Table I (top half) gives
 302 several parameters of importance obtained for each potential. Below, we discuss the most important
 303 results for the EI and LT models. Most results are shown in normalized form to facilitate inter-
 304 comparison: (i) the stress is expressed as the fraction of the Peierls stress, $s = \tau/\tau_P$, (ii) energies
 305 are plotted relative to the zero-stress activation enthalpy ΔH_0 , and (iii) lengths are expressed in
 306 Burgers vector units, b , or Peierls potential wavelength h_0 .

308 A. System length scales: line shapes, kink separation, and kink widths

309 For the sake of clarity, we only show results for the EAM potential in the main body of the text,
 310 and discuss MEAM results in the context of each EAM graph (more discussion provided in Sec. VI
 311 and Appendix D). Figure 7 shows the optimized saddle point configurations for kink pairs as a
 312 function of stress under the EI and LT models for the EAM potential (the configurations obtained
 313 using the MEAM potential is qualitatively similar to those obtained using EAM potential). The
 314 graphs for the EI model results do not show segments LA and DR in their entirety but a diminishing
 315

TABLE I. Interatomic potential-specific parameters. The top half of the table includes atomistic parameters used in the LOS models: a_0 is the lattice constant, τ_P is the Peierls stress, U_{lk} and U_{rk} are the energies of left and right kinks, respectively, and $\Delta H_0 = U_{\text{lk}} + U_{\text{rk}}$ is the zero-stress kink-pair activation enthalpy. The bottom half of the table lists values of parameters extracted from the LOS model calculations, separated between EI and LT calculations: a is the core width, p and q are the exponents of the phenomenological kink-pair enthalpy expressions, ΔH_0^* is the intercept of the kink-pair activation enthalpy with the vertical axis, and τ_a is the stress at which the activation enthalpy vanishes, equivalent to the *athermal* stress in experimental tests.

	EAM		MEAM	
a_0 [Å]	3.19		3.14	
τ_P [GPa]	2.0		3.4	
U_{lk} [eV]	0.71		0.81	
U_{rk} [eV]	0.92		0.99	
ΔH_0 [eV]	1.63		1.80	
	EI	LT	EI	LT
a [b]	0.70	0.80	0.15	0.50
p	0.41	0.83	0.45	0.80
q	1.05	1.38	1.09	1.46
ΔH_0^* [eV]	–	1.68	–	1.84
τ_a [GPa]	1.84	1.99	3.22	3.61

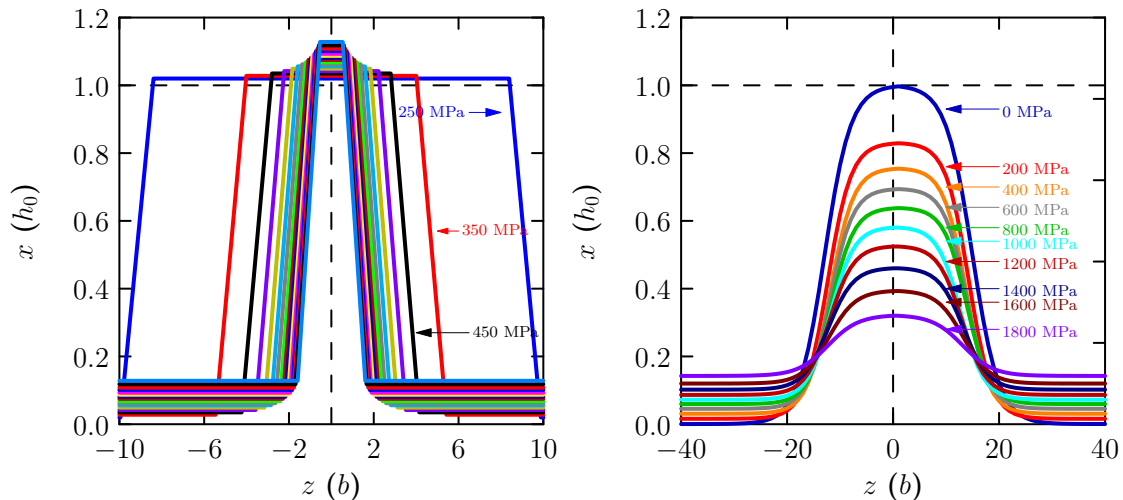
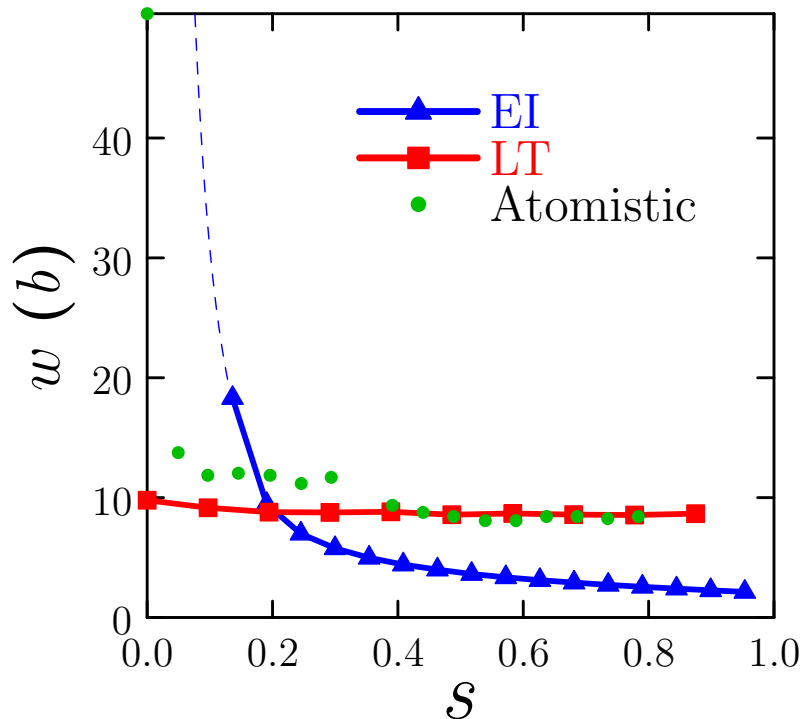


FIG. 7. Optimized kink pair configurations as a function of stress for the EAM potential. (a) Elastic interaction model. (b) Line tension model.

316 kink separation, w , can generally be observed as the stress increases. This variation of w with τ
 317 is plotted in Figure 8. In accordance with elasticity theory, the kink-pair length diverges at zero
 318 stress, decreasing gradually with stress to a final value of $\approx 2b$. For its part, lacking an interaction
 319 energy, the results for w in the LT model are less significant, but they are weakly dependent on
 320 stress. Interestingly, LT predictions for the EAM and MEAM potentials result in differences of
 321 about a factor of two between both atomic models (higher for MEAM). As well, EAM values are

322 in very good agreement with the corresponding atomistic results (around $10b$, from ref. [41]).



323 FIG. 8. Kink separation in the kink-pair under stress (normalized to the corresponding Peierls stress). The
 324 EI results indicate divergence at zero stress, in accordance with elasticity theory, while the LT values are
 325 finite at all stresses. Atomistic results for the EAM potential are shown for comparison, showing very good
 326 agreement with predictions by the LT model.

327 As shown in Fig. 7 for the LT model, the activated state for the dislocation is a bulged config-
 328 uration straddling the Peierls potential. The amplitude of this bulge is plotted in Figure 9 as a
 329 function of stress for the EAM potential. As the figure indicates, this amplitude coincides with the
 330 wavelength of $U_P(x)$, h_0 at zero stress, and is zero at the Peierls stress, consistent with the definition
 331 of the activated state at both ends of the stress range. Our results show excellent agreement with
 332 the expected analytical form for h in line tension models [62, 63] (shown as lines in Fig. 9).

333 While these results are interesting, one of the most important aspects in this work is the asym-
 334 metry in the dislocation core energies introduced in Sec. II 2. This asymmetry manifests itself as
 335 differing kink ‘widths’, i.e. the spreading length along the dislocation line (z -coordinate) of the
 336 segments connecting two consecutive Peierls valleys. These are labeled l_1 and l_2 in Fig. 3. The
 337 results for these two lengths are shown in Figure 10. With the EI model, there are slight differences
 338 between the left and right kinks, with the left one, l_1 , being larger than the right one, l_2 . Contrary
 339 to the situation of the kink-pair separation w , here the EAM kinks spread over approximately twice
 340 the distance of the MEAM ones. These results also show a slow decrease of l_1 and l_2 with stress
 341 (kinks approaching the edge orientation), although interestingly these widths are around $1.5b$ for
 342 the MEAM potential and between 3 and $4b$ for EAM. This stands in contrast to atomistic results,
 which predict kink widths of approximately $25b$ for EAM calculations [41]. For their part, LT

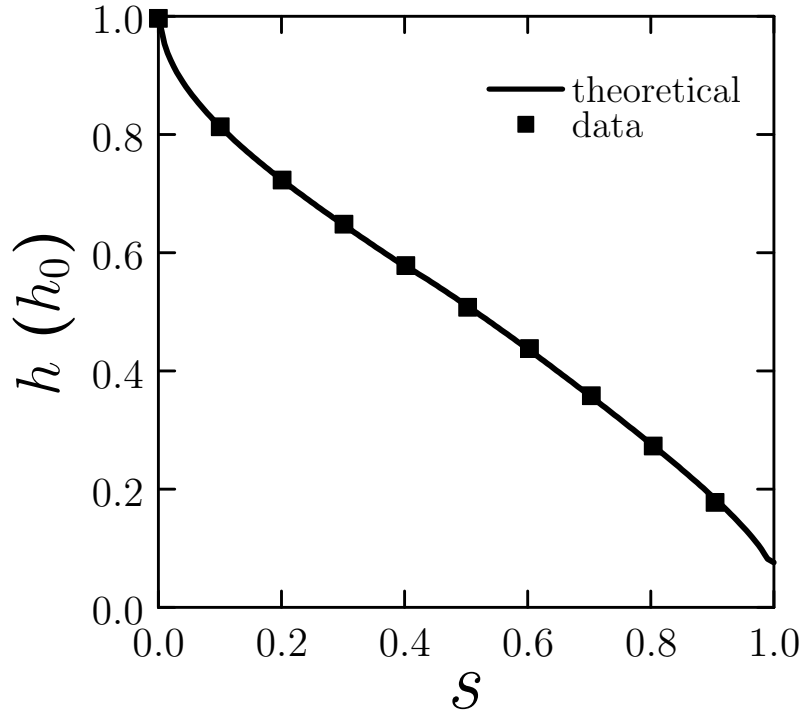


FIG. 9. Amplitude of the saddle-point configuration for the LT model as a function of stress. The results for EAM (black squares) agree well with theoretical predictions [63] (solid line)

343 results show no appreciable difference between l_1 and l_2 . Here too calculations for the EAM po-
 344 tential result in larger kink widths than for the MEAM potential, between 4.5 and $6b$ vs. 3 and $4b$,
 345 respectively. However, l_1 and l_2 display a different dependence with stress in this case, reaching a
 346 minimum at low stresses but growing with stress subsequently.

347

B. System energies: kink energies and activation enthalpies

348 The most important physical quantity to extract from our models is the kink-pair activation
 349 enthalpy as a function of stress. This is used in a number of approaches to describe thermally-
 350 activated screw dislocation motion in bcc metals (as it has been done in our works in the past,
 351 e.g. [41, 64]). In Figure 11 we show the results for the EI and LT models. To facilitate comparison,
 352 we normalize the enthalpies by the unstressed activation enthalpy obtained in atomistic calculations
 353 in each case, ΔH_0 , and the stresses by the Peierls stress τ_P . These parameters are all given in Table
 354 I. Note that (i) the enthalpy at zero stress for the EI model is undefined and therefore the data
 355 point shown in Figure 11 is the atomistic value, and (ii) that the actual intercept of the activation
 356 enthalpy curves for the LT model with the vertical axis does not necessarily correspond to the

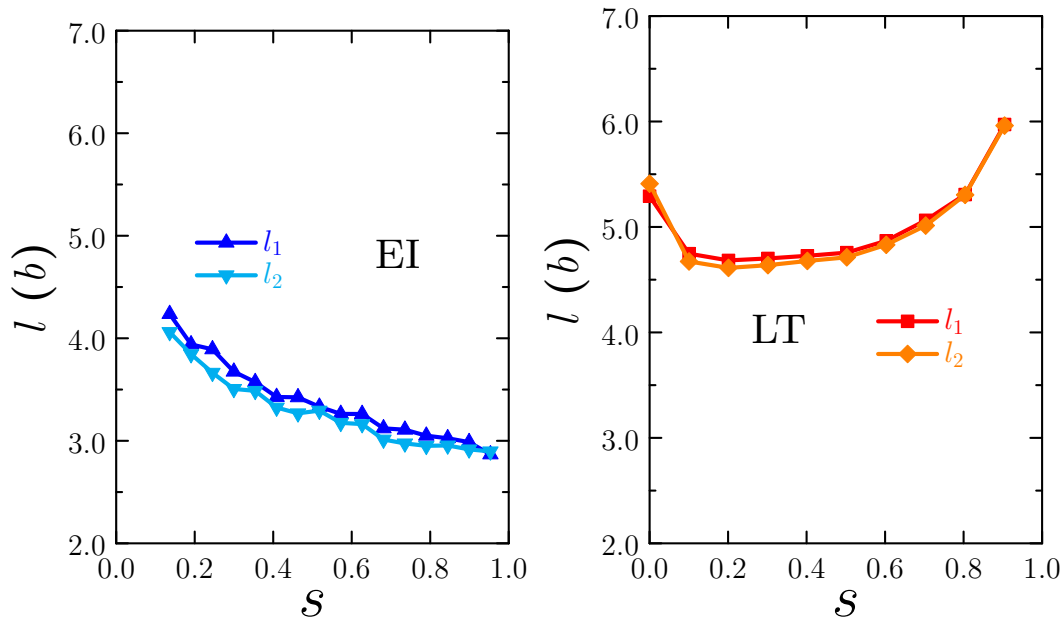


FIG. 10. Kink widths, l_1 and l_2 (refer to Fig. 3), as a function of stress.

357 atomistic value². This is what is labeled as ΔH_0^* in Table I. Similarly, intercepts with the stress
 358 axis in all cases do not necessarily match the value of τ_P , with the actual values labeled as τ_a in
 359 Table I. We interpret these stresses as being the ‘athermal’ limits for the kink-pair mechanism in
 360 each case.

362 Most importantly, the values of a used in eqs. (6), (8), and (18) to obtain these energies have
 363 been chosen as to provide the best fit of the activation enthalpy curves to the known atomistic
 364 values of ΔH_0 and τ_P . In other words, we arbitrarily set the core width value to match known
 365 ‘first-principles’ calculations of the potential in question. These values of a are provided also in
 366 Table I and, as can be seen, are always less than one Burgers vector distance. We will return to
 367 this issue in Sec. VI.

368 Finally, it is common practice to fit the curves in Fig. 11 to the Kocks-Ashby-Argon phenomeno-
 369 logical expression [65]:

$$370 \quad \Delta H(\tau) = \Delta H_0 \left(1 - \left(\frac{\tau}{\tau_P} \right)^p \right)^q \quad (22)$$

371 where p and q are exponents that describe the asymptotic behavior of $\Delta H(\tau)$ in the limits of
 372 zero stress ($q = 1.25$) and the Peierls stress ($p = 0.5$) for isotropic linear elasticity [58]. Since
 373 tungsten is elastically isotropic, our model provides an excellent testbed for these values, which
 374 have indeed been reproduced for stress-independent U_P and symmetric $e_c(\theta, a)$. These exponents

² It is also important to note that ΔH_0 is obtained atomistically via procedures that are insensitive to periodic image interactions [40].

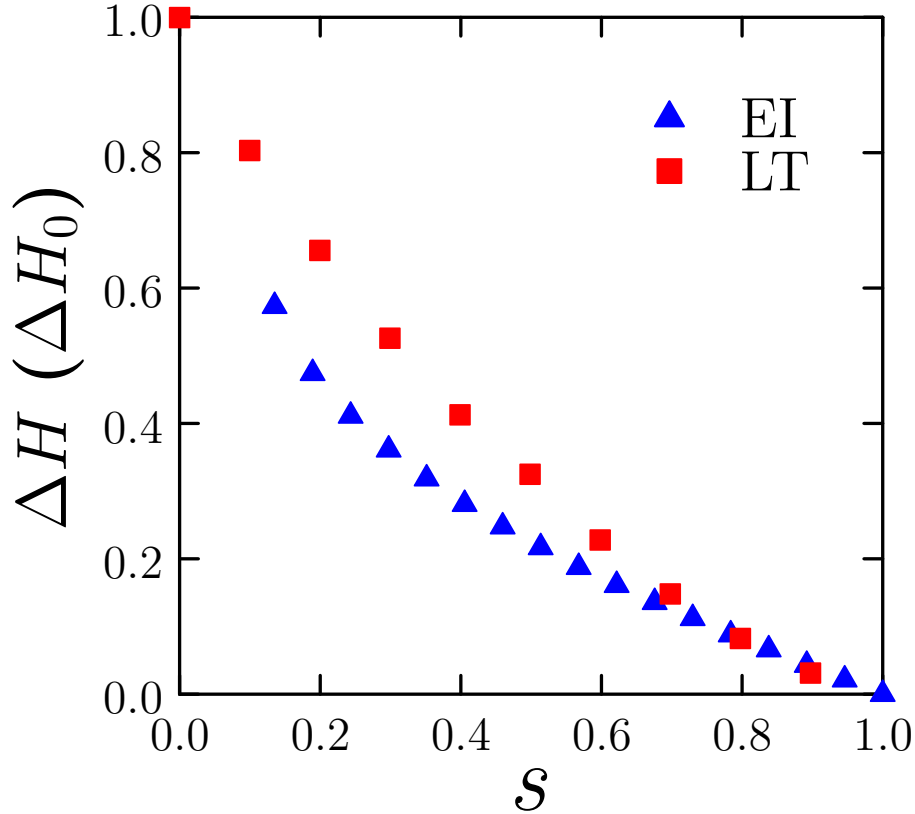


FIG. 11. Kink-pair activation enthalpy for the EI and LT models. The results are normalized to the unstressed activation enthalpy obtained in atomistic calculations and the Peierls stress in each case (refer to Table I).

375 are also provided in Table I. Note that we use eq. (22) only to facilitate comparison across the
 376 atomistic, EI, and LT model results (and for the EAM and MEAM cases) via the values of p and
 377 q , without implying its validity for any specific case.

378 To evaluate again the effect of the core energy asymmetries on the energetics of the activated
 379 states, we calculate in Figure 12 the individual kink energies as a function of τ . As no appreciable
 380 difference was found for the LT model predictions, we omit them from the figure for clarity. The
 381 energies shown include the interaction and self-energies in the EI model of the kink segments only.
 382 Only a noticeable difference can be found for the EAM results, approximately 10%, whereas kinks
 383 energies are practically identical for the MEAM potential. The individual atomistic kink energies
 384 are given in the table above as well (for zero stress), differing about 20% between themselves. We
 385 also discuss this more in depth in the next section.

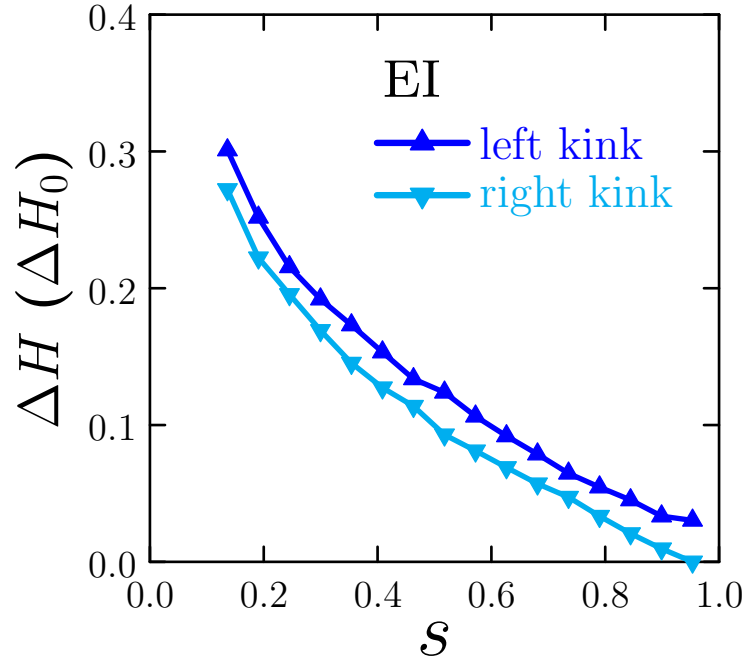


FIG. 12. Energies of individual kinks for LT models for EAM potential. The differences are due to the asymmetry of the core energy functions about the edge orientation.

386

VI. DISCUSSION

387

A. Comparisons between LOS models

388 As indicated in Sec. I, different approximations to the line integral along the x (glide) direction to
 389 calculate the energy of the activated kink-pair state result in different LOS model formulations, each
 390 with its own advantages and disadvantages. The EI model approximates the bulge configuration
 391 better at low stresses, when the activated state extends across the entire Peierls potential period and
 392 the kink-pair energy is dominated by elastic interactions between kink segments. This allows the
 393 use of a simple trapezoidal structure to represent the system, which has the benefit of consisting of
 394 only four degrees of freedom. This considerably speeds up convergence of the energy minimizations,
 395 which allows us to study the parametric space of the model efficiently. The novel aspect of the EI
 396 model used here is the asymmetry of the left and right kinks, by virtue of the character dependence
 397 of the core energy function. Regarding this, the EI model results predict differences of less than 1%
 398 in the kink widths for both EAM and MEAM parameters (Fig. 10), while the difference in enthalpy
 399 is slightly larger (Fig. 12).

400 For its part, the LT model is best suited for lines with small curvature, when the bulge config-
 401 uration is small, a situation typically encountered at high stresses. The implementation of the LT
 402 approach involves, however, up to hundreds of discrete segments, which increases the computational
 403 time severalfold compared to the EI model. LT results show no discernible difference in the values
 404 of both the energies and the kink widths. Thus, it appears that the LT model is less sensitive to

405 the core energy asymmetry than the EI model.

406 In terms of EAM-vs-MEAM differences, as shown in Fig. 11, when normalized to the correspond-
 407 ing values of ΔH_0 and τ_P , the shapes of the LT and EI models differ in less than 3%. This is
 408 an encouraging result as it could potentially indicate that normalized LOS model predictions can
 409 be transferred across different potentials, which would eliminate a common source of variability in
 410 dislocation property calculations.

411 B. Defining the core size by matching LOS models to atomistic data

412 The size of the dislocation core (a in this work) is a mathematical construct introduced to remove
 413 the singularity inherent to the theory of elasticity. As such, it does not possess any intrinsic physical
 414 meaning, serving instead as an arbitrary limit between the elastic and inelastic regions. However,
 415 one can remove some of this arbitrariness by matching the LOS model calculations to atomistic
 416 results of the total energy of kink pair configurations. By adjusting the value of a to partition the
 417 elastic and core energies in eqs. (1) and (20) in such a way as to match the atomistic kink-pair
 418 energies at zero stress (obtained independently for the EAM and MEAM potentials), one can relate
 419 the value of the core width to the size of a region that contains the inelastic contribution to the
 420 total energy. Following these approach, we obtain values of $0.7b$ (EI) and $0.8b$ (LT) for the EAM
 421 case ($\Delta H_0 = 1.63$ eV) and $0.2b$ and $0.5b$ for MEAM ($\Delta H_0 = 1.78$ eV). The fact that these are
 422 between half and a full Burgers vector may be indicative of the order of magnitude to be expected
 423 for this parameter. However, we emphasize that this is one attempt to establish the value of a
 424 using a physical criterion, but it is difficult to ascertain how accurate or valid it is relative to other
 425 approaches [66–68]. In any case, we believe this to be an interesting aspect of our calculations and
 426 worth reporting as an original application of LOS models.

427 C. Building 3D kink-pair models from 2D atomistic data

428 One of the advantages of studying straight dislocations is the existence of translational symmetry
 429 along the line direction, which generally reduces the study of its properties to quasi 2D structures
 430 that need only capture the minimum repeatable translational unit along the dislocation line. For
 431 screw dislocations, this length is of course the Burger’s vector, which is typically the shortest lattice
 432 vector of the crystal. For this reason, general dislocation properties can be efficiently and accurately
 433 calculated using thin atomistic supercells, which makes them amenable to electronic structure
 434 calculations. The existence of kink pairs breaks the translational symmetry of screw dislocations in
 435 bcc (and other) crystals. Being the fundamental structure governing screw dislocation dynamics,
 436 this necessitates using 3D configurations which precludes the use of computationally demanding
 437 approaches such as DFT. Consequently, it has been a goal of the bcc plasticity community to assess
 438 whether 2D information such as what has been presented here (Secs. V A and V B) suffices to capture
 439 3D behavior when incorporated into efficient continuum models of dislocation line configurations.

440 Our calculations provide a testbed for this idea, in line with prior efforts [56], as they allow a
 441 direct comparison to strictly atomistic results of kink-pair configurations using EAM [41, 64]. This
 442 is illustrated in Figure 13, where a good agreement between the LOS results and the atomistic
 443 calculations can be appreciated. As the figure shows, the LT model agrees with the atomistic result
 444 at low stresses, while the EI model produces a better match at high stresses. While this may appear
 445 contradictory with the common assumption that the EI is better suited for low stresses and the LT
 446 model for high stresses, the non-screw segments of the trapezoid in the EI case are highly tilted

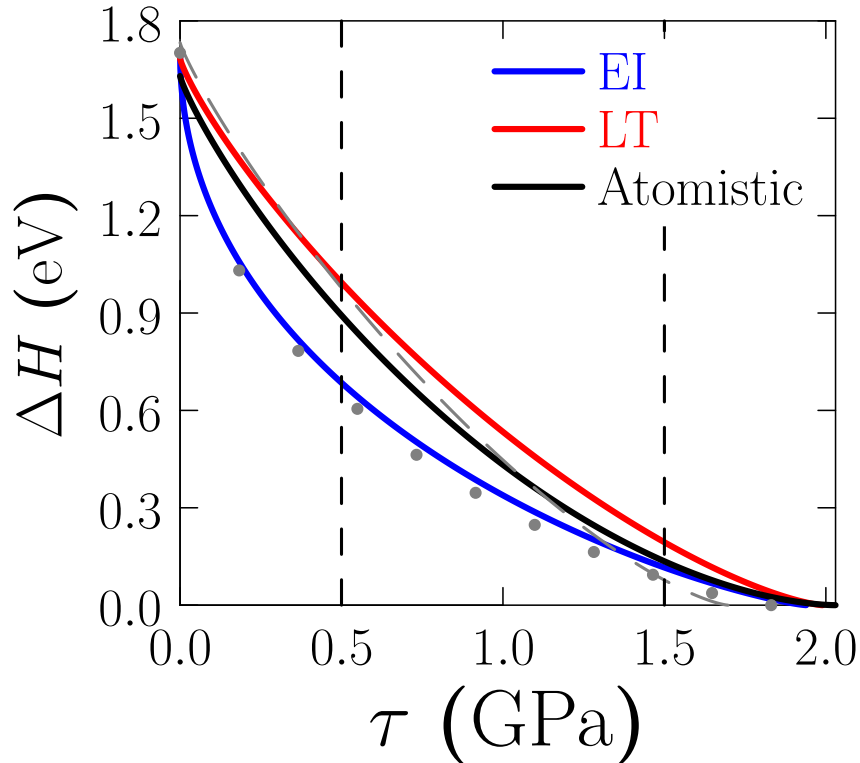


FIG. 13. Comparison of EI, LT, and atomistic models for the EAM potential fitted to eq. (22). The gray dashed line corresponds to LT results assuming no asymmetry in the core energies and no stress-dependence of the Peierls potential ($p = 0.88$, $q = 1.37$), while the gray dotted line is the equivalent EI curve ($p = 0.50$, $q = 1.29$). The vertical dashed lines indicate the limits of the ‘low’ and ‘high’ stress regions, defined *ad hoc* to be at $0.25\sigma_P$ and $0.75\sigma_P$, respectively.

447 towards the screw character due to the combined action of dislocation self and core energies, which
 448 is not unusual in bcc metals. This makes the standard assumption of the EI model weakly true
 449 in this case. For its part, the LT model works well at low stresses not due to the shape of the
 450 kinks but because it provides stable kink-pair configurations at stresses where elastic models do not
 451 converge. Partially, this is because dislocation segments do not interact with one another in the
 452 LT framework, the driving force is only the curvature of the line, which is always minimized for a
 453 given applied stress. At high stresses, the LT fails because the line is ‘bulged’, i.e. it has so much
 454 curvature that the non-interaction assumption starts to fail. In the intermediate stress range, the
 455 EAM calculations lie in between both LOS approaches. Albeit restricted to very specific conditions,
 456 this verification result suggests that continuum models parameterized with atomistic 2D results can
 457 indeed be good approximants of full atomistic behavior in tungsten. While it is not clear how much
 458 of this agreement can be attributed to specific features of W, such as elastic isotropy or the choice
 459 of interatomic potential, we can cautiously conclude that LOS models that employ 2D information
 460 can be trusted to provide acceptable estimates of ΔH in other bcc metals.

D. Discussion of other works

461
 462 Researchers have been calculating kink-pair activation enthalpies using continuum elastic models
 463 since the 1950s. As atomistic information involving fundamental dislocation properties has become
 464 available [54, 60], we have been able to enrich continuum formulations and increase their physical
 465 accuracy. There are several examples of this in the literature [52, 56, 59, 68], each highlighting one
 466 specific aspect of the physics of kink pairs in screw dislocations in bcc metals. However, to the best
 467 of our knowledge, this work constitutes the first LOS formulation to simultaneously integrate (i)
 468 the stress dependence of the Peierls potential, (ii) the asymmetry of the dislocation core energies
 469 with respect to dislocation character, and (iii) the extraction of the core width by matching LOS
 470 results with atomistic results.

VII. CONCLUSIONS

471
 472 Our first conclusion is that one can successfully incorporate atomistic data obtained in quasi-2D
 473 conditions into continuum elastic models of 3D kink-pair configurations. We have demonstrated that
 474 the stress dependence of the Peierls potential and results for core energies as a function of dislocation
 475 character can be integrated into elastic interaction and line tension models in a straightforward
 476 manner. Moreover, we report a slight asymmetry in the core energies about the edge orientation in
 477 W , in accordance with a periodicity of $(0, \pi)$ for the dislocation character space in bcc metals.

478 The asymmetry in the dislocation core energies accounts for no more than 10% difference in left
 479 and right kink energies (compared to no less than 20% in atomistic results) and results in very
 480 slight variations in their spreading lengths. Thus, we conclude that, while they are likely one of
 481 several contributions to this energy asymmetry, core energies alone cannot capture it in its entirety.
 482 However, a representation of core energies in terms of the core width parameter is helpful to extract
 483 the value of this parameter by matching to atomistic data. In our particular case, we find that this
 484 core width is always less than one Burgers vector distance.

485 Including the stress dependence of the Peierls potential in the models appears to shift the athermal
 486 stresses to higher values compared to when just the zero stress potential is used, more in line with
 487 the atomistic values of the Peierls stress. However, this effects is small as well.

488 Finally, our results suggest that atomistic calculations of kink-pair configurations result in acti-
 489 vation enthalpies that are in between elastic interaction and line tension predictions. In particular,
 490 at low stresses atomistic data agree better with line tension calculations, while at high stresses the
 491 agreement is better with full elastic models.

ACKNOWLEDGMENTS

492
 493 The authors thank Dr. Emmanuel Clouet for fruitful discussions. D. C. acknowledges support
 494 from the Engineering HPC at Villanova University. S. H. and J. M. acknowledge support by the
 495 National Science Foundation under Grant DMR-1611342 and the U.S. Department of Energy's Of-
 496 fice of Fusion Energy Sciences, Project DE-SC0012774:0001. Computer time allocations at UCLA's
 497 IDRE Hoffman2 supercomputer are acknowledged.

498

Appendix A: Fitting procedure of the stress dependence of the Peierls potential

499

500

501

502

Here we explain how to introduce the resolved shear-stress dependence in eq. (10). The τ -dependence enters through the parameters U_0 and α and our goal here then is to obtain compact expressions for $U_0(\tau)$ and $\alpha(\tau)$. To this end, we first plot the values of U_0 and α with stress in Figures 14 and 15 for the EAM and MEAM potentials, respectively.

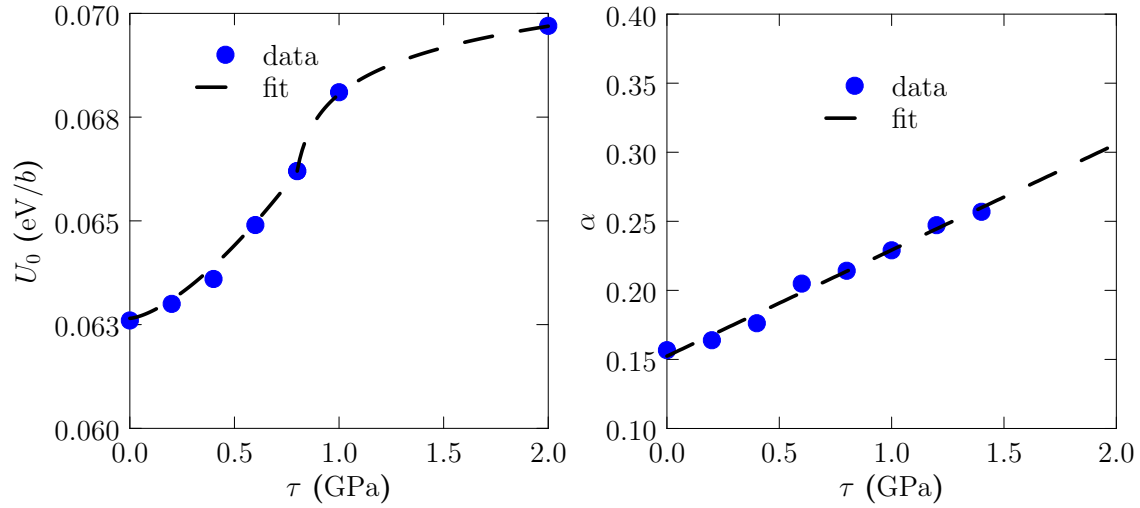


FIG. 14. Fitting of U_0 and α for the EAM potential

503

504

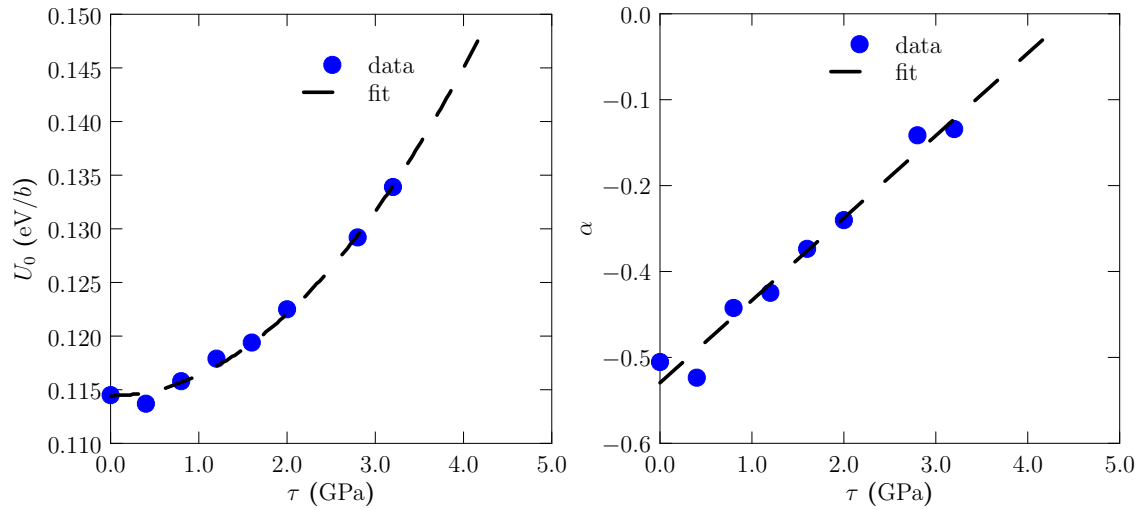


FIG. 15. Fitting of U_0 and α for the MEAM potential

505

As the figures show, generally there is a nonlinear dependence of U_0 with stress and a linear one

506 for α . Consequently, we use power laws for $U_0(\tau)$ and linear relationships for $\alpha(\tau)$.

507 • Fitting of U_0 :

508 – EAM: Due to the change of convexity of the EAM U_0 data, we split the fitting into two
509 regions.

510 1. In the low stress region, $\tau \leq 0.8$ GPa,

$$511 \quad U_0(\tau) = 0.005\tau^{1.49} + 0.06 \quad (\text{A1})$$

512 2. In the high stress region, $\tau > 0.8$ GPa,

$$513 \quad U_0(\tau) = 0.21(\tau - 0.7643)^{0.005} - 0.14 \quad (\text{A2})$$

514 – MEAM:

$$515 \quad U_0(\tau) = 0.003(\tau - 0.13)^{1.6742} + 0.11 \quad (\text{A3})$$

516 with U_0 expressed in [eV/b] when τ is expressed in GPa.

517 • Fitting of α :

518 1. EAM:

$$519 \quad \alpha = 0.077\tau + 0.152 \quad (\text{A4})$$

520 2. MEAM:

$$521 \quad \alpha = 0.115\tau - 0.515 \quad (\text{A5})$$

522 with α non-dimensional when τ is in GPa.

523 We emphasize that these expressions have no implied physical meaning and are simply used for
524 convenience in the range of stresses considered here.

525 Appendix B: Fitting of core energy data

As it was shown in Section II 2, dislocation core energies expressed as:

$$e_c(\theta, a) = f(\theta) + g(\theta) \log\left(\frac{a}{b}\right)$$

where both $f(\theta)$ and $g(\theta)$ are Fourier series of the type:

$$y(\theta) = c_0 + \sum_{k=1}^3 c_k \sin(2i\theta) + d_k \cos(2i\theta)$$

526 Note that this form for $f(\theta)$ and $g(\theta)$ depends only on θ , with the a -dependence contained exclusively
527 in the logarithmic term. This mimics the partition represented by eq. (1). The coefficients in these
528 expressions are obtained by least-squares fitting to the atomistic data points obtained from Fig. 2
529 by varying a and θ , and are listed in Table II. $f(\theta)$ and $g(\theta)$ are plotted as a function of θ in Fig. 16
530 along with the corresponding Fourier series curves for the EAM and MEAM potentials.

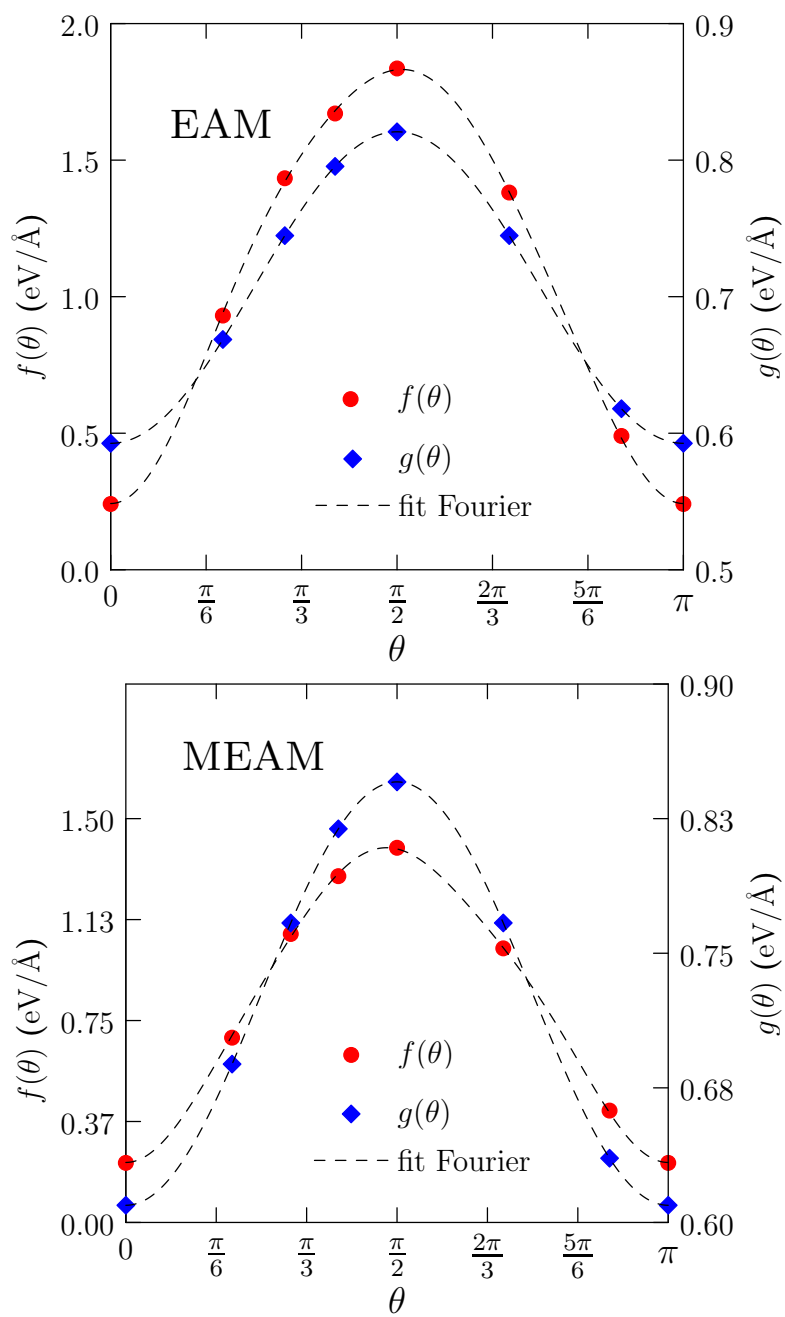


FIG. 16. Dependence of the dislocation core energy terms f and g on dislocation character for (a) EAM and (b) MEAM interatomic potentials.

TABLE II. Values of the Fourier coefficients in eq. (21) for the EAM and MEAM potentials.

Potential	function	c_0	c_1	d_1	c_2	d_2	c_3	d_3
EAM	f	1.1017	0.0149	-0.7895	0.0082	-0.0634	-0.0331	-0.0078
	g	0.7067	-	-0.1141	-	-	-	-
MEAM	f	0.8390	0.0092	-0.5730	-0.0191	-0.0325	-0.0118	-0.0122
	g	0.7275	-	-0.1179	-	-	-	-

531 Appendix C: Expressions of the functional E^* for the interaction energies

532 The functional E^* that appears in the formulation of the interaction energies E_{int} (cf. Section III)
 533 takes different forms depending on the nature of the interaction. In the following, the non-singular
 534 elastic expressions given by Cai *et al.* [53] for parallel and non-parallel segments are provided. In
 535 both cases, the common Burgers vector to both segments is \mathbf{b} .

536 1. Non-parallel segments

537 This is relevant for the interaction between kink segments and screw segments. The energy
 538 functional $E^*(\mathbf{r}) \equiv E_{\text{np}}(\mathbf{r})$ is defined as:

$$\begin{aligned}
 E_{\text{np}}(\mathbf{r}) = & \\
 & \frac{\mu}{4\pi(1-\nu)(\mathbf{u} \cdot \mathbf{u})} \left\{ \mathbf{r} \cdot \ln [R_a + \mathbf{r} \cdot \mathbf{t}'] ((A_1 - A_2)\mathbf{v}' + A_3'\mathbf{u}) + \right. \\
 & + \mathbf{r} \cdot \ln [R_a + \mathbf{r} \cdot \mathbf{t}] ((A_1 - A_2)\mathbf{v} + A_3\mathbf{u}) + A_4 R_a + \\
 & \left. + \frac{(A_1 - A_5) [2(\mathbf{r} \cdot \mathbf{u})^2 + (\mathbf{u} \cdot \mathbf{u})a^2]}{\sqrt{(\mathbf{r} \cdot \mathbf{u})^2 + (\mathbf{u} \cdot \mathbf{u})a^2}} \arctan \left\{ \frac{(1 + \mathbf{t} \cdot \mathbf{t}')R_a + \mathbf{r}(\mathbf{t} + \mathbf{t}')}{\sqrt{(\mathbf{r} \cdot \mathbf{u})^2 + (\mathbf{u} \cdot \mathbf{u})a^2}} \right\} \right\} \quad (\text{C1})
 \end{aligned}$$

where $\mathbf{t} = (\mathbf{r}_2 - \mathbf{r}_1)/L_m$ and $\mathbf{t}' = (\mathbf{r}_4 - \mathbf{r}_3)/L_n$ are the respective line tangents ($L_m = \|\mathbf{r}_2 - \mathbf{r}_1\|$
 and $L_n = \|\mathbf{r}_4 - \mathbf{r}_3\|$), $\mathbf{u} = \mathbf{t} \times \mathbf{t}'$, $\mathbf{v} = \mathbf{u} \times \mathbf{t}$, $\mathbf{v}' = \mathbf{t}' \times \mathbf{u}$, and:

$$R_a = \sqrt{\mathbf{r} \cdot \mathbf{r} + a^2}$$

$$A_1 = (1 + \nu)(\mathbf{b} \cdot \mathbf{t})(\mathbf{b} \cdot \mathbf{t}')$$

$$A_2 = (b^2 + (\mathbf{b} \cdot \mathbf{t})^2)(\mathbf{t} \cdot \mathbf{t}')$$

$$A_2' = (b^2 + (\mathbf{b} \cdot \mathbf{t}')^2)(\mathbf{t} \cdot \mathbf{t}')$$

$$A_3 = 2(\mathbf{b} \cdot \mathbf{u})(\mathbf{b} \cdot \mathbf{v}) \frac{\mathbf{t} \cdot \mathbf{t}'}{\mathbf{u} \cdot \mathbf{u}}$$

$$A'_3 = 2(\mathbf{b} \cdot \mathbf{u})(\mathbf{b} \cdot \mathbf{v}') \frac{\mathbf{t} \cdot \mathbf{t}'}{\mathbf{u} \cdot \mathbf{u}}$$

$$A_4 = ((\mathbf{b} \cdot \mathbf{t})(\mathbf{b} \cdot \mathbf{v}) + (\mathbf{b} \cdot \mathbf{t}')(\mathbf{b} \cdot \mathbf{v}'))(\mathbf{t} \cdot \mathbf{t}')$$

$$A_5 = 2(\mathbf{b} \times \mathbf{u})^2 \frac{\mathbf{t} \cdot \mathbf{t}'}{\mathbf{u} \cdot \mathbf{u}}$$

540 where $b = \|\mathbf{b}\|$. These expressions simplify significantly for perpendicular segments.

541

2. Interaction energy between two parallel segments

542 This interaction includes the interaction of segments of pure screw character with one another
 543 and the interaction of kink segments of the same kind with one another. As above, the Burgers
 544 vector is assumed to be the same for all segments. The interaction energy functional has the form
 545 $E^*(\mathbf{r}) \equiv E_{\parallel}(\mathbf{r})$:

$$546 \quad E_{\parallel}(\mathbf{r}) = \frac{\mu}{4\pi(1-\nu)} \left\{ [2b(\mathbf{b} \cdot \mathbf{r}) - b^2(\mathbf{t} \cdot \mathbf{r})(3-\nu)] \ln \{R_a + \mathbf{t} \cdot \mathbf{r}\} + R_a b^2(2-\nu) + \right. \\ \left. - \frac{R_a}{2} \frac{(\mathbf{b} \cdot \mathbf{r} - b\mathbf{t} \cdot \mathbf{r})^2 - a^2 b^2(\nu-1)}{R_a^2 - (\mathbf{t} \cdot \mathbf{r})^2} \right\} \quad (C2)$$

547 where \mathbf{t} is the common line tangent to both segments.

548

Appendix D: Calculation using MEAM potential

549 Here we show the series of calculations for the MEAM potential. Except for full atomistic
 550 kink-pair enthalpy calculations under stress, the database for the EAM and MEAM potentials is
 551 equivalent. (cf. Table I). Shown are the variation of Peierls potential with stress (in Fig. 17), Fourier
 552 fits of the core energies (Fig. 18), kink separation (in Fig. 19), kink height (Fig. 20), kink widths
 553 (in Fig. 21), and activation enthalpy in Fig. 22

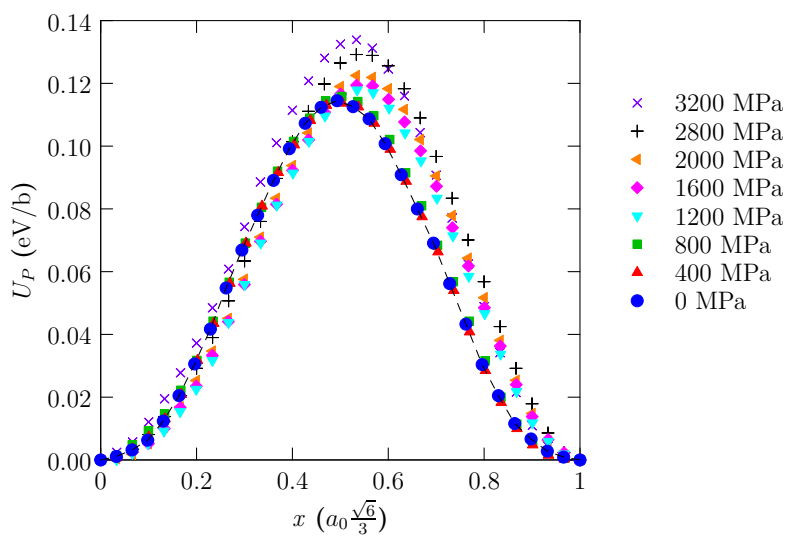


FIG. 17. MEAM potential: Peierls potential variation with stress.

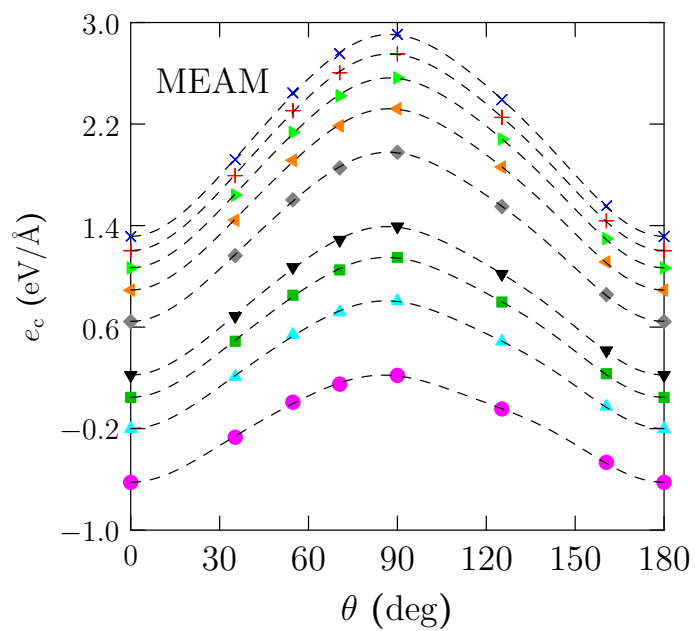


FIG. 18. MEAM potential: Core energy fitting.

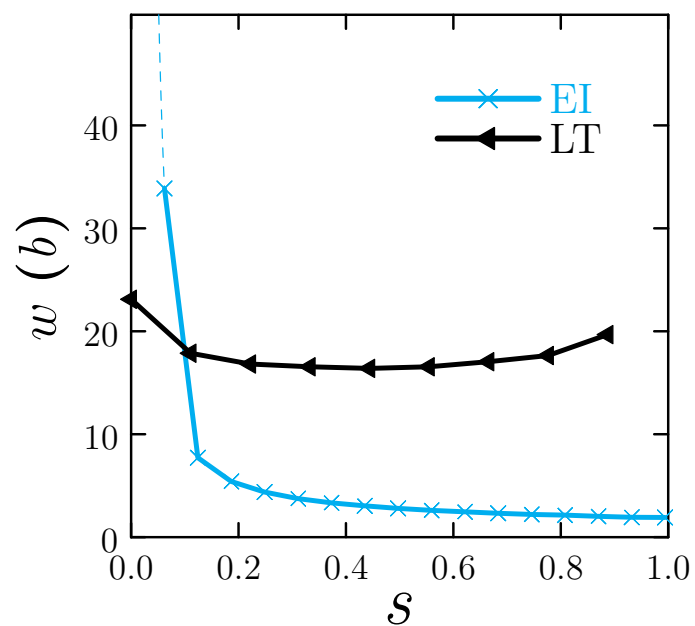


FIG. 19. MEAM potential: Kink separation for EI and LT models

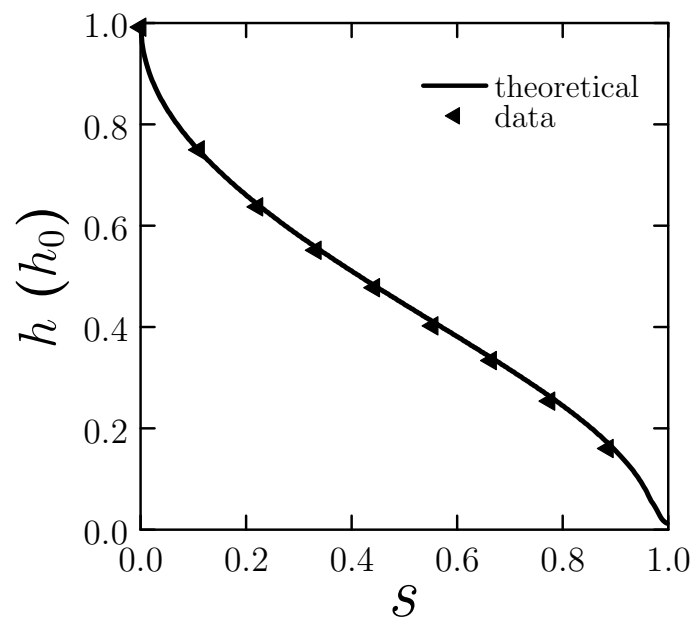


FIG. 20. MEAM potential: Theoretical prediction and simulation results for LT model

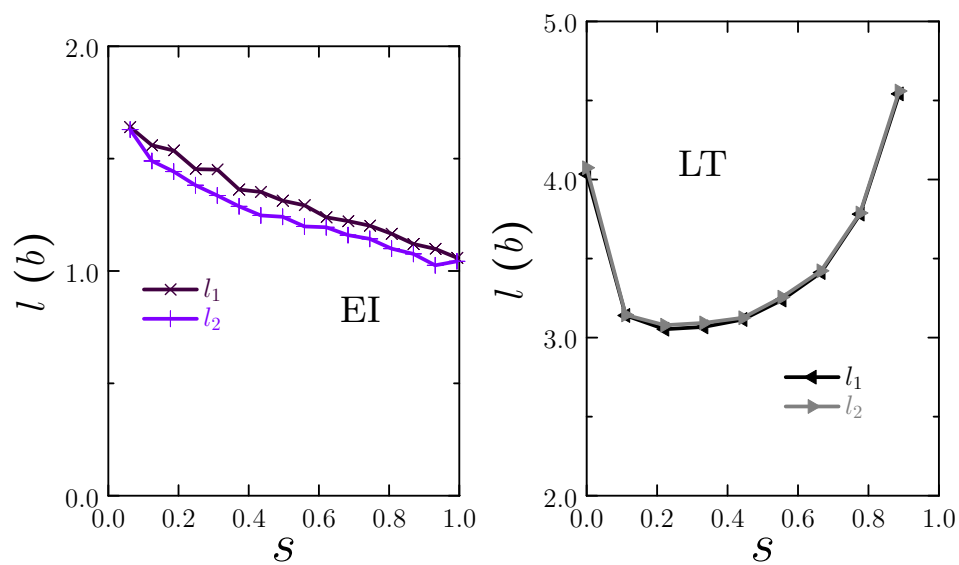


FIG. 21. MEAM potential: Kink widths, l_1 and l_2 as a function of stress

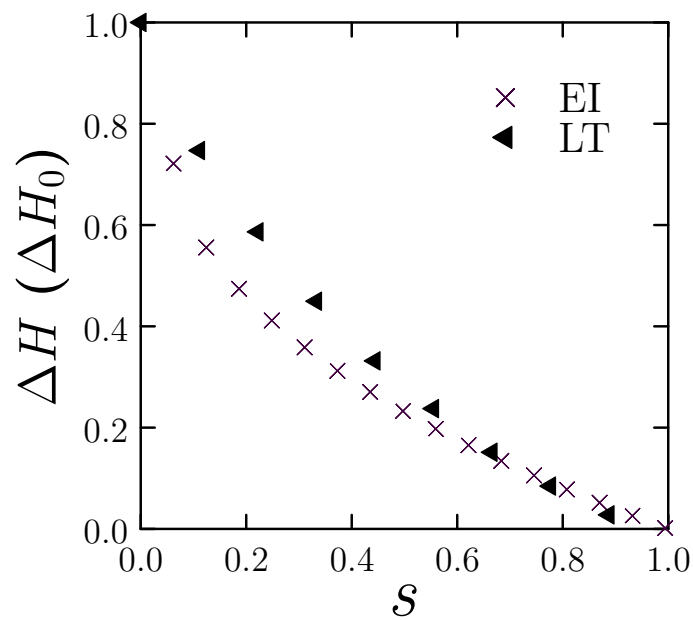


FIG. 22. MEAM potential: Kink-pair activation enthalpy for the EI and LT models.

-
- 556 [1] H. Beladi, Q. Chao, and G. S. Rohrer, *Acta Materialia* **80**, 478 (2014).
557 [2] C. Marichal, H. Van Swygenhoven, S. Van Petegem, and C. Borca, *Scientific Reports* **3** (2013).
558 [3] C. R. Weinberger, B. L. Boyce, and C. C. Battaile, *International Materials Reviews* **58**, 296 (2013),
559 <https://doi.org/10.1179/1743280412Y.0000000015>.
560 [4] J. Bassani, K. Ito, and V. Vitek, *Materials Science and Engineering: A* **319**, 97 (2001).
561 [5] D. Kang, D. Baars, T. Bieler, C. Compton, F. Pourboghrat, and A. Mappar, (2015).
562 [6] A. Seeger and U. Holzwarth, *Philosophical Magazine* **86**, 3861 (2006).
563 [7] O. Barrera, D. Bombac, Y. Chen, T. D. Daff, E. Galindo-Nava, P. Gong, D. Haley, R. Horton,
564 I. Katzarov, J. R. Kermode, C. Liverani, M. Stopher, and F. Sweeney, *Journal of Materials Science*
565 **53**, 6251 (2018).
566 [8] D. Rodney and L. Proville, *Physical Review B* **78**, 104115 (2008).
567 [9] A. Seeger, *Le Journal de Physique IV* **5**, C7 (1995).
568 [10] F. R. Nabarro and M. S. Duesbery, *Dislocations in solids*, Vol. 11 (Elsevier, 2002).
569 [11] Y. Zhao and J. Marian, *Modelling and Simulation in Materials Science and Engineering* **26**, 045002
570 (2018).
571 [12] R. Arsenault, *Acta Metallurgica* **15**, 501 (1967).
572 [13] R. Chang, *Philosophical Magazine* **16**, 1021 (1967).
573 [14] G. Wang, A. Strachan, T. Çağın, and W. A. Goddard III, *Physical Review B* **68**, 224101 (2003).
574 [15] L. Dezerald, D. Rodney, E. Clouet, L. Ventelon, and F. Willaime, *Nature communications* **7**, 11695
575 (2016).
576 [16] R. Gröger and V. Vitek, in *Materials Science Forum*, Vol. 482 (Trans Tech Publ, 2005) pp. 123–126.
577 [17] K. Ito and V. Vitek, *Philosophical Magazine A* **81**, 1387 (2001).
578 [18] M. a.-S. Duesbery and V. Vitek, *Acta Materialia* **46**, 1481 (1998).
579 [19] A. Seeger and W. Wasserbäch, *physica status solidi (a)* **189**, 27 (2002).
580 [20] P. R. Morris and S. Semiatin, *Texture, Stress, and Microstructure* **3**, 113 (1979).
581 [21] C. Marichal, K. Srivastava, D. Weygand, S. V. Petegem, D. Grolimund, P. Gumbsch, and H. V.
582 Swygenhoven, *Physical Review Letters* **113** (2014), [10.1103/physrevlett.113.025501](https://doi.org/10.1103/physrevlett.113.025501).
583 [22] H. Matsui and H. Kimura, *Materials Science and Engineering* **24**, 247 (1976).
584 [23] A. Seeger, *Materials Science and Engineering: A* **319**, 254 (2001).
585 [24] J. E. Sinclair, *Journal of Applied Physics* **42**, 5321 (1971).
586 [25] J. Simmons, S. Rao, and D. Dimiduk, *Philosophical Magazine A* **75**, 1299 (1997).
587 [26] Y. Tang and M. Ouyang, *Nature materials* **6**, 754 (2007).
588 [27] M. R. Gilbert, P. Schuck, B. Sadigh, and J. Marian, *Phys. Rev. Lett.* **111**, 095502 (2013).
589 [28] C. R. Weinberger, G. J. Tucker, and S. M. Foiles, *Phys. Rev. B* **87**, 054114 (2013).
590 [29] H. Huntington, *Proceedings of the Physical Society. Section B* **68**, 1043 (1955).
591 [30] D. Rodney and L. Proville, *Physical Review B* **79**, 094108 (2009).
592 [31] R. Chang and L. Graham, *physica status solidi (b)* **18**, 99 (1966).
593 [32] V. Celli, M. Kabler, T. Ninomiya, and R. Thomson, *Physical Review* **131**, 58 (1963).
594 [33] P. Guyot and J. E. Dorn, *Canadian Journal of Physics* **45**, 983 (1967).
595 [34] K. Edagawa, T. Suzuki, and S. Takeuchi, *Physical Review B* **55**, 6180 (1997).
596 [35] J. E. Dorn, J. Mitchell, and F. Hauser, *Experimental mechanics* **5**, 353 (1965).
597 [36] J. P. Hirth and J. Lothe, (1982).
598 [37] H. Koizumi, H. Kirchner, and T. Suzuki, *Acta Metallurgica et Materialia* **41**, 3483 (1993).
599 [38] H. Koizumi, H. O. Kirchner, and T. Suzuki, *Philosophical Magazine A* **69**, 805 (1994).
600 [39] L. Proville, L. Ventelon, and D. Rodney, *Physical Review B* **87**, 144106 (2013).
601 [40] L. Ventelon, F. Willaime, and P. Leyronnas, *Journal of Nuclear Materials* **386**, 26 (2009).
602 [41] A. Stukowski, D. Cereceda, T. D. Swinburne, and J. Marian, *International Journal of Plasticity* **65**,

- 603 108 (2015).
- 604 [42] T. Swinburne, S. Dudarev, S. Fitzgerald, M. Gilbert, and A. Sutton, *Physical Review B* **87**, 064108
605 (2013).
- 606 [43] D. Cereceda, A. Stukowski, M. Gilbert, S. Queyreau, L. Ventelon, M.-C. Marinica, J. Perlado, and
607 J. Marian, *Journal of Physics: Condensed Matter* **25**, 085702 (2013).
- 608 [44] M.-C. Marinica, L. Ventelon, M. Gilbert, L. Proville, S. Dudarev, J. Marian, G. Bencteux, and
609 F. Willaime, *Journal of Physics: Condensed Matter* **25**, 395502 (2013).
- 610 [45] H. Park, M. R. Fellingner, T. J. Lenosky, W. W. Tipton, D. R. Trinkle, S. P. Rudin, C. Woodward,
611 J. W. Wilkins, and R. G. Hennig, *Physical Review B* **85**, 214121 (2012).
- 612 [46] G. Henkelman, G. Jhannesson, and H. Jonsson, *Methods for Finding Saddle Points and Minimum*
613 *Energy Paths* (Kluwer Academic Publishers, 2000) Chap. 10, pp. pages 269 – 300.
- 614 [47] S. Plimpton, *Journal Of Computational Physics* **117**, 1 (1995).
- 615 [48] T. Arias and J. Joannopoulos, *Physical review letters* **73**, 680 (1994).
- 616 [49] W. Cai, V. V. Bulatov, J. Chang, J. Li, and S. Yip, *Physical Review Letters* **86**, 5727 (2001).
- 617 [50] W. Cai, V. V. Bulatov, J. Chang, J. Li, and S. Yip, *Philosophical Magazine* **83**, 539 (2003).
- 618 [51] M. Hossain and J. Marian, *Acta Materialia* **80**, 107 (2014).
- 619 [52] K. Kang, V. V. Bulatov, and W. Cai, [Proceedings of the National Academy of Sciences](https://www.pnas.org/content/109/38/15174.full.pdf) **109**, 15174
620 (2012), <https://www.pnas.org/content/109/38/15174.full.pdf>.
- 621 [53] W. Cai, A. Arsenlis, C. R. Weinberger, and V. V. Bulatov, *Journal of the Mechanics and Physics of*
622 *Solids* **54**, 561 (2006).
- 623 [54] C. R. Weinberger, G. J. Tucker, and S. M. Foiles, *Physical Review B* **87**, 054114 (2013).
- 624 [55] L. Dezerald, L. Ventelon, E. Clouet, C. Denoual, D. Rodney, and F. Willaime, *Physical Review B* **89**,
625 024104 (2014).
- 626 [56] L. Dezerald, L. Proville, L. Ventelon, F. Willaime, and D. Rodney, *Physical Review B* **91**, 094105
627 (2015).
- 628 [57] A. Brailsford, *Physical Review* **139**, A1813 (1965).
- 629 [58] D. Caillard and J.-L. Martin, *Thermally activated mechanisms in crystal plasticity*, Vol. 8 (Elsevier,
630 2003).
- 631 [59] L. Proville, L. Ventelon, and D. Rodney, [Phys. Rev. B](https://doi.org/10.1103/PhysRevB.87.144106) **87**, 144106 (2013).
- 632 [60] X. W. Zhou, R. B. Sills, D. K. Ward, and R. A. Karnesky, *Physical Review B* **95**, 054112 (2017).
- 633 [61] W. H. Press, B. P. Flannery, S. A. Teukolsky, and W. T. Vetterling, *Cambridge University Press* **78**,
634 134 (1990).
- 635 [62] S. Fitzgerald, *Scientific reports* **6**, 39708 (2016).
- 636 [63] V. P. Zhdanov, *Physics Letters A* (2018).
- 637 [64] D. Cereceda, M. Diehl, F. Roters, D. Raabe, J. M. Perlado, and J. Marian, *International Journal of*
638 *Plasticity* **78**, 242 (2016).
- 639 [65] U. Kocks, A. Argon, and M. Ashby, *Progress in Materials Science* **19** (1975), cited By 69.
- 640 [66] C. Sawyer, J. Morris Jr, and D. Chrzan, *Physical Review B* **87**, 134106 (2013).
- 641 [67] S. Das and V. Gavini, *Journal of the Mechanics and Physics of Solids* **104**, 115 (2017).
- 642 [68] P.-A. Geslin and D. Rodney, *Physical Review B* **98**, 174115 (2018).